



Final Technical Report
ONR Grant N00014-14-1-0827

Assessment of CFD Modeling Capability for
Hypersonic Shock Wave Boundary Layer Interactions

30 November 2015

Doyle Knight
Dept Mechanical and Aerospace Engineering
Rutgers, The State University of New Jersey
98 Brett Road · Piscataway, NJ 08854
Email: doyleknight@gmx.com · Tel: 732 762 5510

20151207010

REPORT DOCUMENTATION PAGE					Form Approved OMB No. 0704-0188	
<p>The public reporting burden for this collection of information is estimated to average 1 hour per response, including the time for reviewing instructions, searching existing data sources, gathering and maintaining the data needed, and completing and reviewing the collection of information. Send comments regarding this burden estimate or any other aspect of this collection of information, including suggestions for reducing the burden, to Department of Defense, Washington Headquarters Services, Directorate for Information Operations and Reports (0704-0188), 1215 Jefferson Davis Highway, Suite 1204, Arlington, VA 22202-4302. Respondents should be aware that notwithstanding any other provision of law, no person shall be subject to any penalty for failing to comply with a collection of information if it does not display a currently valid OMB control number.</p> <p>PLEASE DO NOT RETURN YOUR FORM TO THE ABOVE ADDRESS.</p>						
1. REPORT DATE (DD-MM-YYYY)		2. REPORT TYPE		3. DATES COVERED (From - To)		
30-11-2015		Final Technical Report		26 May 2014 - 30 September 2015		
4. TITLE AND SUBTITLE Assessment of CFD Modeling Capability for Hypersonic Shock Wave Boundary Layer Interactions				5a. CONTRACT NUMBER		
				5b. GRANT NUMBER N00014-14-1-0827		
				5c. PROGRAM ELEMENT NUMBER		
6. AUTHOR(S) Doyle Knight				5d. PROJECT NUMBER		
				5e. TASK NUMBER		
				5f. WORK UNIT NUMBER		
7. PERFORMING ORGANIZATION NAME(S) AND ADDRESS(ES) Rutgers, The State University of New Jersey Office of Research and Sponsored Programs 3 Rutgers Plaza, ASB III New Brunswick, NJ 08901-8559				8. PERFORMING ORGANIZATION REPORT NUMBER n/a		
9. SPONSORING/MONITORING AGENCY NAME(S) AND ADDRESS(ES) Office of Naval Research 875 North Randolph Street Arlington, VA 22203-1995				10. SPONSOR/MONITOR'S ACRONYM(S)		
				11. SPONSOR/MONITOR'S REPORT NUMBER(S)		
12. DISTRIBUTION/AVAILABILITY STATEMENT Unclassified, Distribution Unlimited						
13. SUPPLEMENTARY NOTES						
14. ABSTRACT The report assesses the capability of Computational Fluid Dynamics to predict the aerothermodynamic loads on simplified geometries in hypersonic flight. The specific configurations are the double cone and hollow cylinder flare. Experiments conducted at the Calspan University of Buffalo Research Center (CUBRC) at Mach 10.9 to 13.2 and stagnation enthalpies from 5 MJ/kg to 22 MJ/kg. Simulations were performed using the laminar compressible Navier-Stokes equations and both perfect gas and Park I thermochemistry models. The Park I model demonstrated reliable results for peak heat transfer at all conditions; however, the predictions using Park I for peak pressure and separation length were unreliable.						
15. SUBJECT TERMS Shock waves, boundary layers, Computational Fluid Dynamics (CFD), hypersonic, aerothermodynamics						
16. SECURITY CLASSIFICATION OF:			17. LIMITATION OF ABSTRACT	18. NUMBER OF PAGES	19a. NAME OF RESPONSIBLE PERSON	
a. REPORT	b. ABSTRACT	c. THIS PAGE			Doyle Knight	
UU	UU	UU	UU	45	19b. TELEPHONE NUMBER (Include area code) 848 445 4464	

Final Technical Report

Assessment of CFD Modeling Capability
for Hypersonic Shock Wave Boundary Layer
ONR Grant N00014-14-1-0827

Period of Grant: 26 May 2014 - 30 September 2015

Professor Doyle Knight
Department of Mechanical and Aerospace Engineering
Rutgers University - The State University of New Jersey
98 Brett Road · Piscataway, New Jersey 08854
Tel: 732 762 5510 · Fax: 732 445 3124
Email: doyleknight@gmx.com

Submitted to:
Mr. Gil Graff
Office of Naval Research
875 N Randolph, Room 1129
Arlington, VA 22203
Phone: 703 588 0703 · Fax: 703 696 4274
Email: gil.graff@navy.mil

30 November 2015

Contents

1	Introduction	5
2	Description of Experiments	6
3	Methodology	9
3.1	Perfect Gas Laminar Navier-Stokes	9
3.2	Non-equilibrium Laminar Navier-Stokes	9
3.3	Numerical Algorithm	13
4	Results	15
4.1	Double Cone	15
4.1.1	5.44 MJ/kg (Run 1)	16
4.1.2	9.65 MJ/kg (Run 2)	16
4.1.3	15.23 MJ/kg (Run 6)	17
4.1.4	21.77 MJ/kg (Run 4)	17
4.1.5	Analysis of Flowfield	22
4.2	Hollow Cylinder Flare	27
4.2.1	5.07 MJ/kg (Run 1)	27
4.2.2	10.43 MJ/kg (Run 2)	27
4.2.3	15.54 MJ/kg (Run 4)	27
4.2.4	21.85 MJ/kg (Run 5)	28
4.2.5	Analysis of Flowfield	32
5	Conclusions, Significance of Results and Transitions	40
6	Personnel	41
7	Publications	41
7.1	Conference Papers	41
7.2	Journal Papers	42
7.3	Other	42

8 Point of Contact	42
9 Acknowledgment and Disclaimer	42
10 Metrics	42

Abstract

The report assesses the capability of Computational Fluid Dynamics to predict the aerothermodynamic loads on simplified geometries in hypersonic flight. The specific configurations selected are the double cone and hollow cylinder flare. Experiments were previously conducted at the Calspan University of Buffalo Research Center (CUBRC) at stagnation enthalpies from 5 MJ/kg to 22 MJ/kg in air and Mach numbers from 10.9 to 13.2. Experimental diagnostics include surface pressure and heat transfer. Laminar compressible Navier-Stokes simulations were performed using both perfect gas and non-equilibrium Park I thermochemistry models. Detailed grid refinement studies were performed to establish the accuracy of the simulations. The principal conclusions of the research are

- The Park I model accurately predicts the peak heat flux $\max Q_w$ in nearly all cases
- The Park I model accurately predicts the separation length L_{sep} and peak pressure $\max p$ in approximately one-half of the cases
- The perfect gas model accurately predicts the peak heat flux $\max Q_w$ in all four hollow cylinder flare cases, but in none of the double cone cases
- The perfect gas model accurately predicts the separation length L_{sep} in one case and peak pressure $\max p$ in none of the cases

The significance of the results is:

- The Park I model is a reliable model for prediction of peak heat flux
- The Park I model is not a reliable model for prediction of peak surface pressure or separation length (*i.e.*, surface pressure distribution)
- The perfect gas model is not a reliable model for prediction of peak surface pressure or separation length (*i.e.*, surface pressure distribution) except at the lowest stagnation enthalpy
- The perfect gas model is not a reliable model for prediction of peak heat flux except at the lowest stagnation enthalpy; it is accurate for hollow cylinder flare at all stagnation enthalpies, but not for the double cone

The significance is limited to the types of shock wave laminar boundary layer interactions considered in this study.

1 Introduction

The design of effective high speed (*e.g.*, hypersonic) weapons systems requires accurate modeling of the influence of the flow on the vehicle performance. In particular, the interaction of shock waves and boundary layers leads to a variety of critical flow phenomena including high heat transfer at reattachment, flow separation resulting in significant changes to the surface pressure (and hence forces and moments on the vehicle), and unsteadiness causing dynamic aerothermodynamic loads. Thus, accurate modeling of shock wave boundary layer interaction is essential.

Shock wave boundary layer interaction has been studied since the 1940s. One of the earliest experiments was performed by Liepmann[1] examining the interactions of a shock wave on a twelve percent circular arc airfoil at Mach 0.8 for both laminar and turbulent boundary layers. Schlieren imaging (Fig. 1) and surface pressure measurements indicated a significant effect of the boundary layer state (*i.e.*, laminar *vs* turbulent).

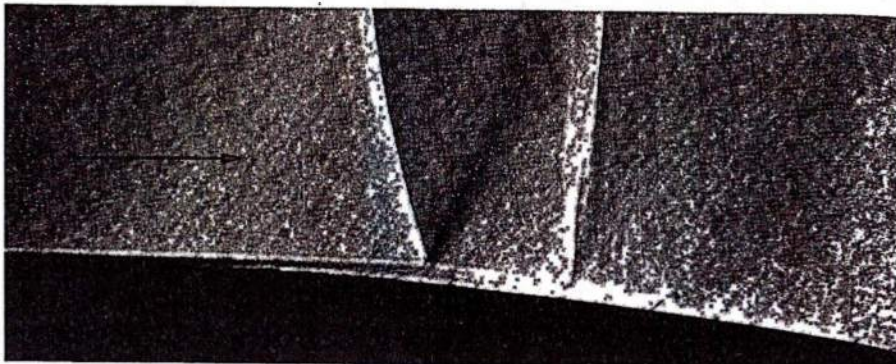


Figure 1: Shock wave boundary layer interaction [1] at Mach 0.863

Beginning in the late 1960s, Computational Fluid Dynamics (CFD) emerged as a separate branch of fluid mechanics research. Early on significant effort was focused on simulation of high speed flows, in particular, shock wave boundary layer interaction (*e.g.*, MacCormack [2], Shang *et al* [3], Hung and MacCormack [4]). Beginning in the early 1990s, CFD modeling of shock wave boundary layer interactions had progressed to a degree sufficient to warrant detailed assessment by NATO AGARD. An early assessment was performed by AGARD Working Group 18 (1992-1997) focusing on shock wave boundary layer interaction at supersonic speeds. Laminar and turbulent boundary layers were considered. Only RANS models were considered in the latter case. The study highlighted the failure of RANS model predictions of skin friction and heat transfer (Knight and Degrez [5]).

AGARD Working Group 10 (1998-2003) continued evaluation of supersonic shock wave turbulent boundary layer interactions. Modeling was extended to include LES and DNS (for nominal two-dimensional, low Reynolds number interactions) and RANS (for three-dimensional interactions). The former showed significant progress in predictive capability;

however, no comparison with surface heat transfer was performed and the Reynolds numbers considered were not representative of conditions for modern air vehicles. The RANS models failed to accurately predict heat transfer (Knight *et al* [6]).

RTO AVT Task Group 136 (2004-2008) extended the focus to hypersonic laminar shock wave boundary layer interactions in non-equilibrium flows. Two configurations were considered – a double cone model at Mach 11.6 in N_2 at stagnation enthalpies of 5.3 MJ/kg and 9.7 MJ/kg, and a cylinder in air at Mach 9 at stagnation enthalpies of 13.5 MJ and 22.4 MJ/kg. CFD capability for prediction of surface heat transfer and pressure for the double cone was mixed; poor agreement with surface heat transfer on the cylinder at the highest enthalpy was observed (Knight *et al* [7]).

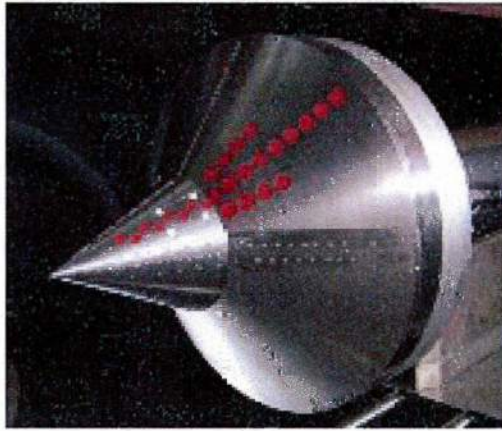
STO AVT Task Group 205 (2011-2014) focused on hypersonic laminar shock boundary layer interaction and hypersonic boundary layer transition caused by a single protuberance. CFD simulations of a nominally double wedge configuration identified the limitations of the experiment. In particular, the experimental surface heat transfer did not represent the fully steady state flow, and the experimental flowfield was evidently three-dimensional. (Knight and Chazot [8]).

In summary, the results of several previous assessments of CFD capability for modeling hypersonic shock wave boundary layer interaction (in particular, for laminar boundary layers at high stagnation enthalpies) is inconclusive.

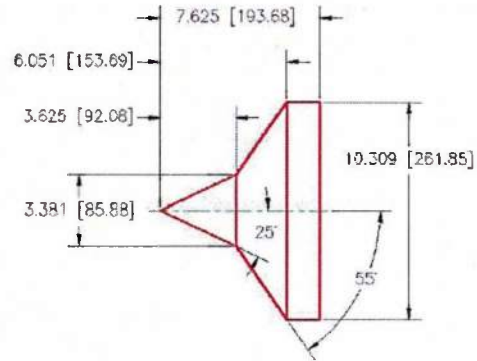
The principal objective of this project was to assess CFD modeling capability for hypersonic shock wave laminar boundary layer interactions. Two experimental configurations were selected – the double cone and hollow cylinder flare models tested at the Calspan University of Buffalo Research Center (CUBRC) at stagnation enthalpies from 5 MJ/kg to 22 MJ/kg in air and Mach numbers from 10.9 to 13.2. Experimental diagnostics include surface pressure and heat transfer. Laminar compressible Navier-Stokes simulations were performed using both perfect gas and non-equilibrium Park I thermochemistry models. Detailed grid refinement studies were performed to establish the accuracy of the simulations.

2 Description of Experiments

An extensive set of experiments were performed at Calspan University of Buffalo Research Center (CUBRC) under the direction of Dr. Michael Holden to examine the effects of thermochemistry in shock wave laminar boundary layer interactions. Two separate configurations were considered – the double cone (Fig. 2) and the hollow cylinder flare (Fig. 3). The experiments were performed in the LENS XX facility. A description of the facility is presented in Dufrene *et al* [9, 10]. The inflow gas was air in full chemical and thermochemical equilibrium with mass fractions of 0.765 and 0.235 for N_2 and O_2 , respectively. The model surface was isothermal at 300 K. The inflow conditions for the double cone and hollow cylinder flare experiments are listed in Tables 1 and 2, respectively.



(a) Photograph

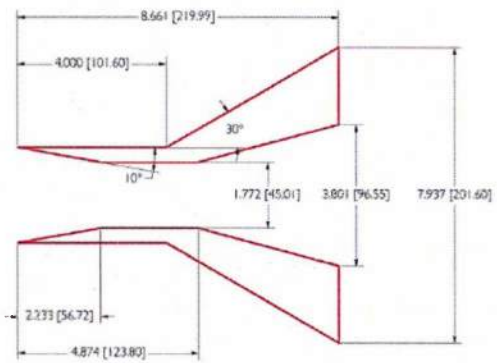


(b) Drawing

Figure 2: Double Cone (dimensions in inches [mm])



(a) Photograph



(b) Drawing

Figure 3: Hollow Cylinder Flare (dimensions in inches [mm])

Experimental diagnostics included surface heat transfer and pressure. A total of 24 pressure transducers and 50 heat flux gauges were installed in the double cone model, and 19 pressure transducers and 52 heat flux gauges in the hollow cylinder flare model. The pressure transducer is 6 mm diameter. The heat flux gauge is a strip whose dimension in the streamwise direction is less than 0.1 mm. Approximately 7% of the pressure transducer data and 4% to 12% of the heat transfer data was not used. The experimental uncertainty for heat flux and pressure measurements is $\pm 10\%$ [11].

Table 1: Flow Conditions for Double Cone Experiments

Run No.	Total Enthalpy (MJ/kg)	Mach Number	Pitot Pressure (kPa)	Unit Reynolds Number $/10^6(\text{m}^{-1})$	Velocity (km/s)	Density (g/m^3)	Temperature (K)
---------	------------------------	-------------	----------------------	---------------------------------------------	-----------------	-----------------------------------	-----------------

1	5.44	12.2	5.1	0.14	3.246	0.499	175
2	9.65	10.90	17.5	0.19	4.303	0.984	389
6	15.23	11.46	59.0	0.39	5.466	2.045	573
4	21.77	12.82	39.5	0.20	6.497	0.964	652

NOTE: "Run No." corresponds to the experimental run identification number

Table 2: Flow Conditions for Hollow Cylinder Flare Experiments

Run No.	Total Enthalpy (MJ/kg)	Mach Number	Pitot Pressure (kPa)	Unit Reynolds $(/10^6 \text{ m}^{-1})$	Velocity (km/s)	Density (gm/m^3)	Temperature (K)
---------	------------------------	-------------	----------------------	----------------------------------------	-----------------	------------------------------------	-----------------

1	5.07	11.3	5.9	0.15	3.123	0.634	189
2	10.43	12.6	9.7	0.12	4.497	0.499	318
4	15.54	11.5	64.0	0.42	5.470	2.216	569
5	21.85	13.2	39.0	0.20	6.515	0.947	618

NOTE: "Run No." corresponds to the experimental run identification number

In comparing the computed heat transfer and pressure with experiment, it is important to relate the computational grid spacing along the surface to the sensor size. The streamwise length of the heat sensor is less than $100\mu\text{m}$, and the diameter of the pressure sensor is 6 mm. The grid resolution of the simulations in the vicinity of the peak pressure is typically $79.5\mu\text{m}$ (1M cells) and $40\mu\text{m}$ (4M cells). Thus, the grid spacing along the surface is comparable to the size of the heat transfer sensor, but significantly smaller than the diameter of the pressure sensor. The width of the symbols used for the surface pressure graphs in Section 4 are approximately the size of the pressure sensor, and thus it is possible to visually "average" the computed pressure distribution over the size of the pressure sensor.

A separate extensive set of experiments were performed at CUBRC to examine the shock wave turbulent boundary layer interactions under equilibrium conditions in the range Mach 5 to 8 for a cone flare and hollow cylinder flare of length 2.50 m and 2.79 m, respectively. Preliminary computations were performed for the hollow cylinder flare geometry at one test condition; however, the computational requirements for the simulation significantly exceeded the available resources at Rutgers University, and therefore efforts were focused on a full study of the two laminar shock wave boundary layer interaction configurations described above at four test conditions each.

3 Methodology

Navier-Stokes simulations were performed for the double cone and hollow cylinder using two different thermochemistry models – perfect gas and Park I [12].

3.1 Perfect Gas Laminar Navier-Stokes

The governing equations are the laminar Navier-Stokes equations for a perfect gas. Using the Einstein summation notation,

$$\frac{\partial \rho}{\partial t} + \frac{\partial \rho u_j}{\partial x_j} = 0 \quad (1)$$

$$\frac{\partial \rho u_i}{\partial t} + \frac{\partial \rho u_i u_j}{\partial x_j} = -\frac{\partial p}{\partial x_i} + \frac{\partial \tau_{ij}}{\partial x_j} \quad (2)$$

$$\frac{\partial \rho \varepsilon}{\partial t} + \frac{\partial}{\partial x_j} (\rho \varepsilon + p) u_j = -\frac{\partial q_j}{\partial x_j} + \frac{\partial \tau_{ij} u_i}{\partial x_j} \quad (3)$$

$$p = \rho RT \quad (4)$$

where the total energy per unit mass ε is

$$\varepsilon = e + \frac{1}{2} u_j u_j \quad (5)$$

where the internal energy per unit mass e is

$$e = c_v T \quad (6)$$

and the heat flux vector and laminar viscous stress tensor are

$$q_j = -k \frac{\partial T}{\partial x_j} \quad (7)$$

$$\tau_{ij} = -\frac{2}{3} \mu \frac{\partial u_k}{\partial x_k} \delta_{ij} + \mu \left(\frac{\partial u_i}{\partial x_j} + \frac{\partial u_j}{\partial x_i} \right) \quad (8)$$

The molecular viscosity μ is defined by Sutherland's Law and the molecular Prandtl number $Pr = \mu c_p / k$ is 0.72. The gas constant $R = 287$ J/kg·K for air.

3.2 Non-equilibrium Laminar Navier-Stokes

We consider a reacting mixture of gases with density ρ_α for $\alpha = 1, \dots, n$ of which $\alpha = 1, \dots, m$ constitute diatomic (or polyatomic) species and the remainder ($i = m + 1, \dots, n$) represent monatomic species.

Conservation of Mass

The conservation of mass is

$$\frac{\partial \rho_\alpha}{\partial t} + \frac{\partial \rho_\alpha u_j}{\partial x_j} = \dot{\omega}_\alpha^{\text{spe}} + \frac{\partial}{\partial x_j} \left[\rho D \frac{\partial Y_\alpha}{\partial x_j} \right] \quad \text{for } \alpha = 1, \dots, n \quad (9)$$

where ρ_α is the density of species α , the mass-averaged velocity is u_j , and ρ is the mixture density

$$\rho = \sum_{\alpha=1}^N \rho_\alpha \quad (10)$$

The mass fraction is defined as

$$Y_\alpha = \frac{\rho_\alpha}{\rho} \quad (11)$$

The rate of production of species α is denoted as $\dot{\omega}_\alpha^{\text{spe}}$ and defined as

$$\dot{\omega}_\alpha^{\text{spe}} = \mathcal{M}_\alpha \sum_{j=1}^J (\nu''_{\alpha,j} - \nu'_{\alpha,j}) k_{f,j} \left[\prod_{l=1}^n \left(\frac{\rho_l}{\mathcal{M}_l} \right)^{\nu'_{\alpha,l}} - \frac{1}{k_{e,j}} \prod_{l=1}^n \left(\frac{\rho_l}{\mathcal{M}_l} \right)^{\nu''_{\alpha,l}} \right] \quad \text{for } \alpha = 1, \dots, n \quad (12)$$

for the general reaction expressions

$$\nu'_{1,j} X_1 + \dots + \nu'_{n,j} X_n \rightleftharpoons \nu''_{1,j} X_1 + \dots + \nu''_{n,j} X_n \quad \text{for } j = 1, \dots, J \quad (13)$$

where J is the number of reactions, and $\nu'_{\alpha,j}$ and $\nu''_{\alpha,j}$ are the stoichiometric coefficients of the reactants and species X_α in the j^{th} reaction.

The diffusion of species is modeled by Fick's Law assuming a uniform diffusivity D defined by

$$D = \frac{\mu}{\rho Sc} \quad (14)$$

where $Sc = 0.7$ is the constant Schmidt number and μ is the molecular viscosity defined by Sutherland's Law or Svehla and McBride [13].

Conservation of Momentum

The conservation of momentum is

$$\frac{\partial \rho u_i}{\partial t} + \frac{\partial \rho u_i u_j}{\partial x_j} = -\frac{\partial p}{\partial x_i} + \frac{\partial \tau_{ij}}{\partial x_j} \quad \text{for } i = 1, 2, 3 \quad (15)$$

where τ_{ij} is the laminar viscous stress tensor defined by Eq (8).

Conservation of Total Energy

The total energy per unit mass ε is the sum of the internal energy per unit mass e and the kinetic energy per unit mass

$$\varepsilon = e + \frac{1}{2} u_j u_j \quad (16)$$

The internal energy per unit mass e is the sum of the internal energies of each of the n species

$$e = \sum_{\alpha=1}^n \frac{\rho_{\alpha}}{\rho} e_{\alpha} \quad (17)$$

where the internal energy per unit mass of each species e_{α} is the sum of an equilibrium internal energy $e_{\alpha}^{\text{eq}}(T)$ due to random translational energy and rotational energy (in the case of molecules) at a bulk equilibrium temperature T and a non-equilibrium internal energy $e_{\alpha}^{\text{vib}}(T_{\alpha}^{\text{vib}})$ due to vibrational excitation (in the case of molecules)

$$e_{\alpha} = e_{\alpha}^{\text{eq}}(T) + e_{\alpha}^{\text{vib}}(T_{\alpha}^{\text{vib}}) \quad (18)$$

The equilibrium internal energy of species α is

$$e_{\alpha}^{\text{eq}}(T) = h_{f_{\alpha}}^{\circ} + \int_{T_{\text{ref}}}^T c_{v_{\alpha}}(T) dT \quad (19)$$

The conservation of total energy is

$$\frac{\partial \rho \varepsilon}{\partial t} + \frac{\partial}{\partial x_j} (\rho \varepsilon + p) u_j = \frac{\partial \tau_{ij} u_i}{\partial x_j} - \frac{\partial q_j}{\partial x_j} \quad (20)$$

where the heat transfer vector is defined by

$$q_j = -k \frac{\partial T}{\partial x_j} - \sum_{\alpha=1}^m k_{\alpha}^{\text{vib}} \frac{\partial T_{\alpha}^{\text{vib}}}{\partial x_j} - \sum_{\alpha=1}^n \rho h_{\alpha} D_{\alpha} \frac{\partial Y_{\alpha}}{\partial x_j} \quad (21)$$

The static enthalpy per unit mass for species α is

$$h_{\alpha} = h_{f_{\alpha}}^{\circ} + \int_{T_{\text{ref}}}^T c_{p_{\alpha}}(T) dT \quad (22)$$

where $h_{f_{\alpha}}^{\circ}$ is the enthalpy of formation of species α at T_{ref} .

Conservation of Vibrational Energy

The conservation of vibrational energy is

$$\frac{\partial \rho e_{\alpha}^{\text{vib}}}{\partial t} + \frac{\partial \rho e_{\alpha}^{\text{vib}} u_j}{\partial x_j} = - \frac{\partial q_{\alpha j}^{\text{vib}}}{\partial x_j} + \dot{\omega}_{\alpha}^{\text{vib}} \quad \text{for } \alpha = 1, \dots, m \quad (23)$$

The heat transfer vector is

$$q_{\alpha j}^{\text{vib}} = -k_{\alpha}^{\text{vib}} \frac{\partial T_{\alpha}^{\text{vib}}}{\partial x_j} - \rho D_{\alpha} e_{\alpha}^{\text{vib}} \frac{\partial Y_{\alpha}}{\partial x_j} \quad (24)$$

The source term is

$$\dot{\omega}_{\alpha}^{\text{vib}} = \rho_{\alpha} \dot{e}_{\alpha}^{\text{vib}} + \dot{\omega}_{\alpha}^{\text{spe}} e_{\alpha}^{\text{vib}} \quad (25)$$

where $\dot{e}_\alpha^{\text{vib}}$ is the translational-vibrational energy transfer per unit mass of species α defined by the Landau-Teller model [14]

$$\dot{e}_\alpha^{\text{vib}} = \frac{e_\alpha^{\text{vib}*}(T) - e_\alpha^{\text{vib}}(T_\alpha^{\text{vib}})}{\tau_\alpha} \quad (26)$$

where $e_\alpha^{\text{vib}*}$ is the equilibrium vibrational energy per unit mass of species α defined by

$$e_\alpha^{\text{vib}*}(T) = \sum_{n=1}^{N_{\Theta,\alpha}} \frac{R_\alpha \Theta_\alpha^{\text{vib}(n)}}{\exp(\Theta_\alpha^{\text{vib}(n)}/T) - 1} \quad (27)$$

and $N_{\Theta,\alpha}$ is the number of characteristic temperatures $\Theta_\alpha^{\text{vib}(n)}$ and τ_α is the relaxation time [15] of species α defined by

$$\tau_\alpha = \frac{\sum_{\beta=1}^n M_\beta}{\sum_{\beta=1}^n M_\beta \tau_{\alpha\beta}^{-1}} \quad (28)$$

where $M_\alpha = \rho_\alpha/\mathcal{M}_\alpha$ is the molar concentration of species α and $\tau_{\alpha\beta}$ is the characteristic relaxation time of species α resulting from collisions with species β defined by[15]

$$\tau_{\alpha\beta} = \frac{1}{p} \exp \left[A_{\alpha\beta} \left(T^{-\frac{1}{3}} - B_{\alpha\beta} \right) - 18.42 \right] \quad \text{atm-s} \quad (29)$$

where

$$A_{\alpha\beta} = 0.00116 \mathcal{M}_{\alpha\beta}^{\frac{1}{2}} \Theta_\alpha^{\text{vib}\frac{4}{3}} \quad \text{and} \quad B_{\alpha\beta} = 0.015 \mathcal{M}_{\alpha\beta}^{\frac{1}{4}} \quad (30)$$

and the averaged molecular weight is defined by

$$\mathcal{M}_{\alpha\beta} = \frac{\mathcal{M}_\alpha \mathcal{M}_\beta}{\mathcal{M}_\alpha + \mathcal{M}_\beta} \quad (31)$$

Equation of State

The equation of state is

$$p = T \sum_{\alpha=1}^n \rho_\alpha R_\alpha \quad (32)$$

where the gas constant R_α for species α is

$$R_\alpha = \frac{\mathcal{R}}{\mathcal{M}_\alpha} \quad (33)$$

where \mathcal{R} is the Universal Gas Constant and \mathcal{M}_α is the molecular weight of species α .

Thermochemistry Model

The non-equilibrium Navier-Stokes simulations used the thermochemistry model proposed by Park[12] comprising five species (N_2 , O_2 , NO , N , O) and seventeen reactions (Table 3).

Table 3: Thermochemistry Model Reactions

Reaction	C ($\text{m}^3/\text{kg}\cdot\text{mole}\cdot\text{s}$)	η	ϵ/k (K)	α	β	A_1	A_2	A_3	A_4	A_5
$N_2 + N_2 \rightarrow N + N + N_2$	$3.70 \cdot 10^{18}$	-1.6	113200	0.5	0.5	10.81	-12.61	0.683	-0.118	0.006
$N_2 + N \rightarrow N + N + N$	$1.11 \cdot 10^{19}$	-1.6	113200	0.5	0.5	10.81	-12.61	0.683	-0.118	0.006
$N_2 + NO \rightarrow N + N + NO$	$3.70 \cdot 10^{18}$	-1.6	113200	0.5	0.5	10.81	-12.61	0.683	-0.118	0.006
$N_2 + O_2 \rightarrow N + N + O_2$	$3.70 \cdot 10^{18}$	-1.6	113200	0.5	0.5	10.81	-12.61	0.683	-0.118	0.006
$N_2 + O \rightarrow N + N + O$	$1.11 \cdot 10^{19}$	-1.6	113200	0.5	0.5	10.81	-12.61	0.683	-0.118	0.006
$N_2 + O \rightarrow NO + N$	$3.18 \cdot 10^{10}$	0.1	37700	1.0	0.0	2.349	-4.828	0.455	-0.075	0.004
$O_2 + N_2 \rightarrow O + O + N_2$	$2.75 \cdot 10^{16}$	-1.0	59500	0.5	0.5	8.243	-4.127	-0.616	0.093	-0.005
$O_2 + N \rightarrow O + O + N$	$8.25 \cdot 10^{16}$	-1.0	59500	0.5	0.5	8.243	-4.127	-0.616	0.093	-0.005
$O_2 + NO \rightarrow O + O + NO$	$2.75 \cdot 10^{16}$	-1.0	59500	0.5	0.5	8.243	-4.127	-0.616	0.093	-0.005
$O_2 + O_2 \rightarrow O + O + O_2$	$2.75 \cdot 10^{16}$	-1.0	59500	0.5	0.5	8.243	-4.127	-0.616	0.093	-0.005
$O_2 + O \rightarrow O + O + O$	$8.25 \cdot 10^{16}$	-1.0	59500	0.5	0.5	8.243	-4.127	-0.616	0.093	-0.005
$NO + O \rightarrow N + O_2$	$2.16 \cdot 10^5$	1.29	19220	1.0	0.0	0.215	-3.657	0.843	-0.136	0.007
$NO + N_2 \rightarrow N + O + N_2$	$2.30 \cdot 10^{14}$	-0.5	75500	0.5	0.5	8.457	-7.784	0.228	-0.043	0.002
$NO + NO \rightarrow N + O + NO$	$2.30 \cdot 10^{14}$	-0.5	75500	0.5	0.5	8.457	-7.784	0.228	-0.043	0.002
$NO + O_2 \rightarrow N + O + O_2$	$2.30 \cdot 10^{14}$	-0.5	75500	0.5	0.5	8.457	-7.784	0.228	-0.043	0.002
$NO + N \rightarrow N + O + N$	$4.60 \cdot 10^{14}$	-0.5	75500	0.5	0.5	8.457	-7.784	0.228	-0.043	0.002
$NO + O \rightarrow N + O + O$	$4.60 \cdot 10^{14}$	-0.5	75500	0.5	0.5	8.457	-7.784	0.228	-0.043	0.002

NOTES

$$k_f = C T_a^\eta e^{-\epsilon/k T_a}, \quad T_a = T^\alpha T_{\text{vib}}^\beta, \quad k_e = \exp(A_1 + A_2 z + A_3 z^2 + A_4 z^3 + A_5 z^4) \text{ where } z = 10^4/T$$

3.3 Numerical Algorithm

The perfect gas laminar Navier-Stokes equations were solved using the GASPex software [16], and the non-equilibrium laminar Navier-Stokes equations using the Park I model were solved using the GASP software [16]. The inviscid fluxes were discretized using either the algorithm of Roe [17], Van Leer [18] or HLLE [19] with Min-Mode reconstruction. Viscous fluxes were discretized using central differencing.

A multi-zone block-structured grid was generated for both configurations. The computational domains are shown in Fig. 4 and 5. For the double cone, axisymmetry conditions are applied from A to B, and symmetry conditions on C to D. Inflow boundary conditions are applied from B to C, and from D to G. No slip boundary conditions are applied on H to A with fixed wall temperature and no surface reactions (for Park I model simulations¹). Zero gradient boundary conditions are applied on G to H. For the hollow cylinder flare, the boundary conditions are extrapolation from A to B, inflow from B to C, symmetry from C to D, inflow from D to E, symmetry from E to F, inflow from F to G, symmetry from G to H, extrapolation from H to I, isothermal no-slip wall from I to J and then to A.

For the double cone, typically two computations were performed for each configuration and inflow condition. The first grid was typically 1 M cells, and the second grid was 4 M or 5.3 M cells. For the hollow cylinder flare, three computations were performed for each perfect gas simulation (except for the 21.85 MJ/kg case) at 1 M, 4.2 M and 16.7 M cells. Two simulations were performed using the Park I for the 10.43 MJ/kg, 15.54 MJ/kg and 21.85 MJ/kg cases

¹A separate simulation was performed using air catalysis boundary conditions on the boundary H to A and the results were essentially identical to the no surface reaction case.

with 1 M and 4 M cells.

The simulations were initialized using the freestream conditions and converged to steady state using Gauss-Seidel iteration or Dual Time Stepping [16]. Computations were performed on 48 or 128 core Linux clusters in the Department of Mechanical and Aerospace Engineering, and on 112 core Linux cluster in the School of Engineering.

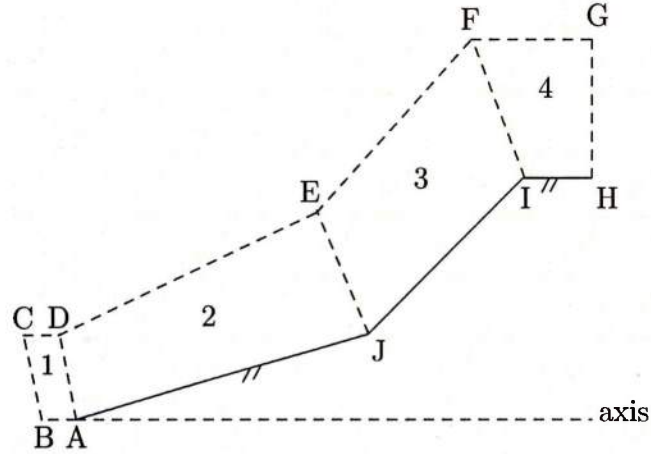


Figure 4: Double Cone

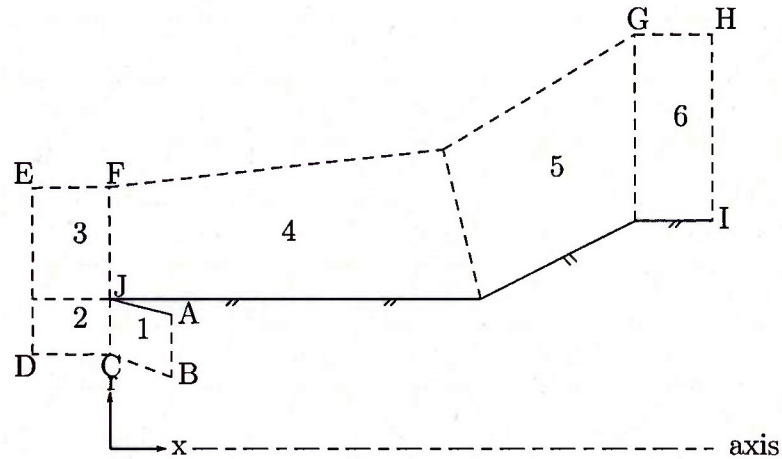


Figure 5: Hollow Cylinder Flare

4 Results

An extensive series of simulations were performed for the double cone and hollow cylinder flare geometries using both the perfect gas and Park I thermochemistry models. Additionally, a grid refinement study was performed for selected cases to assess the accuracy of the simulations. The results are presented below.

4.1 Double Cone

Perfect gas and Park I thermochemistry model simulations were performed for all four experimental test conditions listed in Table 1. Details are presented in Table 4.

Table 4: Double Cone Simulations

Run No	Total Enthalpy (MJ/kg)	Mach Number	Perfect Gas		Park I	
			1M	4M	1.3M	5.3M
1	5.44	12.2	✓	✓	✓	
2	9.65	10.9	✓		✓	
6	15.23	11.46	✓		✓	✓
4	21.77	12.82	✓		✓	

The basic flowfield structure for 21.77 MJ/kg (Run 4) is displayed in Fig. 6 for reference in comparison of the experiment and simulations. A detailed discussion of the flowfield structure is presented later.

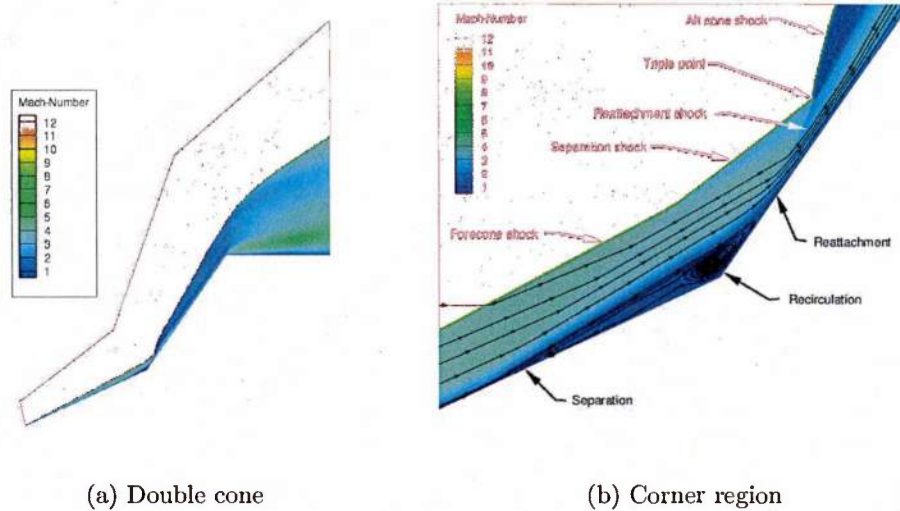


Figure 6: Mach contours for double cone using Park I (21.77 MJ/kg)

4.1.1 5.44 MJ/kg (Run 1)

The computed and experimental heat transfer and surface pressure for 5.44 MJ/kg (Run 1) using the perfect gas and Park I models are presented in Fig. 8. The perfect gas and Park I results are in generally close agreement with each other for both surface pressure and heat transfer except for the location of the peak heat transfer and peak pressure. The computed heat transfer upstream of the separation point at $x = 7$ cm slightly underpredicts the experiment. The location of separation as defined by the drop in Q_w is accurately predicted by both models.

The computed peak heat transfer and pressure overestimate the experiment by 40% and 60%, respectively, for the perfect gas model. The computed peak heat transfer for the Park I model is within the experimental uncertainty; however, the computed peak pressure for the Park I model is 55% above the experiment.

A grid refinement study was performed for 5.44 MJ/kg (Run 1) using the perfect gas model. Results for the 1 M and 4 M cell grids (Fig. 8) are virtually identical, with the maximum difference in peak heat transfer and peak pressure between the two grid solutions of 6% and 3%, respectively.

4.1.2 9.65 MJ/kg (Run 2)

The computed and experimental heat transfer and surface pressure for 9.65 MJ/kg (Run 2) using the perfect gas and Park I models are presented in Fig. 9. The perfect gas results show significant disagreement with the experiment. The streamwise length of the separated region is overpredicted by 75%. The magnitude of the peak heat transfer is in good agreement with experimental peak heat transfer; however, the location is shifted downstream by 1.5 cm. The Park I results show closer agreement with experiment than the perfect gas simulations, although significant differences are evident. The streamwise length of the separation region is underpredicted by 40%. The peak heat transfer is predicted within 15%, while the computed peak pressure is 30% greater than the peak experimental pressure.

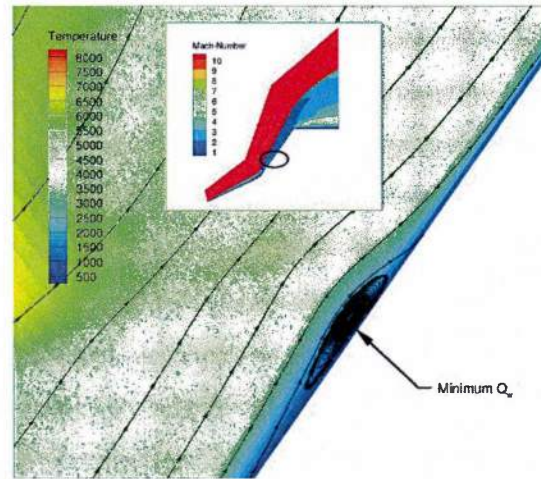


Figure 7: Temperature contours (Park I)

The dramatic drop and rise in the computed heat transfer at $x = 10.05$ cm using Park I is a real physical phenomenon in the simulation. The numerical grid spacing along the surface in this region (see inset in Fig. 9(d)) indicates a careful resolution of the heat transfer profile. This phenomenon is associated with the formation of a small recirculation bubble on the wall as seen in Fig. 7.

4.1.3 15.23 MJ/kg (Run 6)

The computed and experimental heat transfer and surface pressure for 15.23 MJ/kg (Run 6) using the perfect gas and Park I models are presented in Fig. 10. Similar to the 9.65 MJ/kg case, the perfect gas results show significant disagreement with the experiment. The streamwise length of the separation region and the peak heat transfer are both overpredicted by 100%.

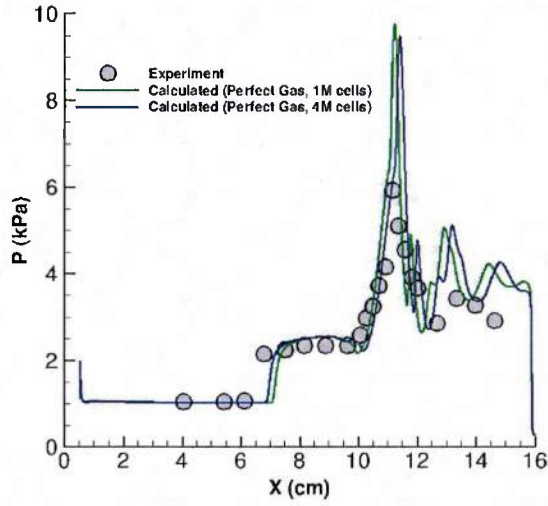
The Park I results show closer agreement with experiment than the perfect gas simulations, although significant differences are evident as seen previously for the 9.65 MJ/kg case. The streamwise length of the separation region is underpredicted by 50%. The magnitude of the peak heat transfer is accurately predicted.

A grid refinement study was performed for 15.23 MJ/kg (Run 6) using the Park I model. Results for the 1.3M and 5.3M cell cases show very close agreement (Fig. 10).

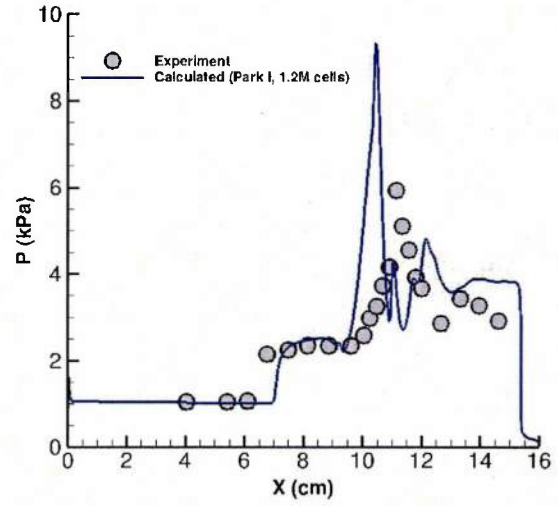
The Park I heat transfer and pressure profiles display a dramatic drop and rise at $x = 10.05$ cm similar to the 9.65 MJ/kg case. The phenomenon is captured by both the 1.3M and 5.3M cell grid systems. The behavior is attributable to the formation of a small recirculation bubble on the surface near reattachment.

4.1.4 21.77 MJ/kg (Run 4)

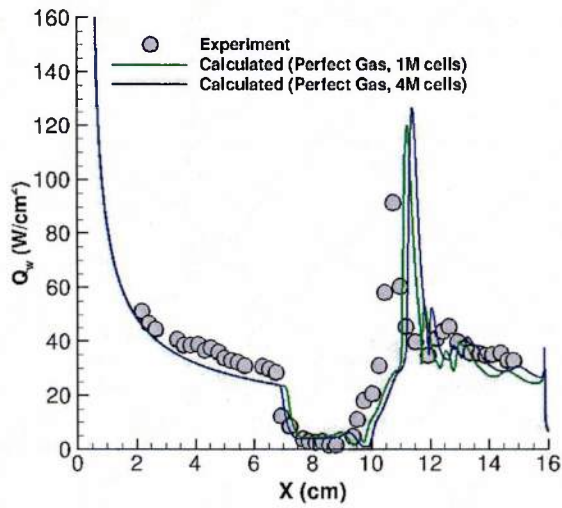
The computed and experimental heat transfer and surface pressure for 21.77 MJ/kg using the perfect gas and Park I models are presented in Fig. 11. Similar to the 9.65 MJ/kg and 15.23 MJ/kg cases, the perfect gas results show significant disagreement with the experiment. The streamwise length of the separation region and the magnitude of the peak heat transfer are overpredicted by 100%. The Park I results show closer agreement with experiment than the perfect gas simulations, although minor differences are evident. The streamwise length of the separation region is accurately predicted, together with the magnitude of the peak heat transfer and peak pressure.



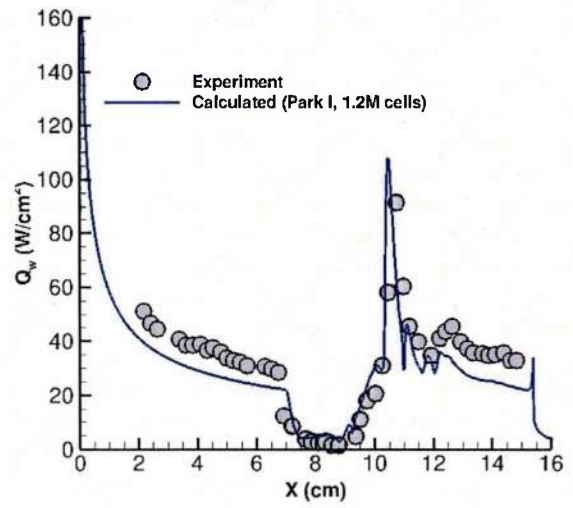
(a) Pressure (perfect gas)



(b) Pressure (Park I)

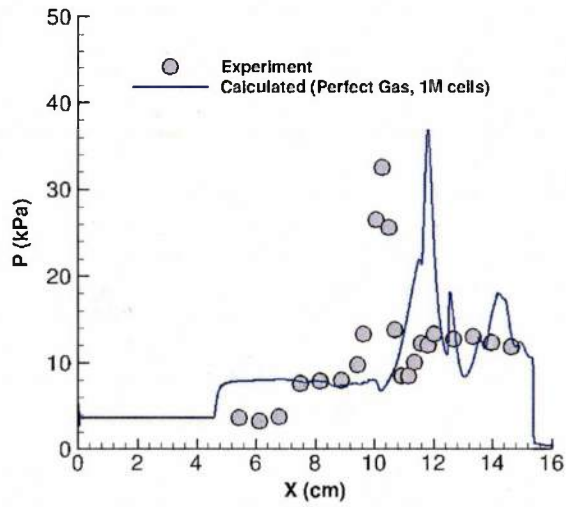


(c) Heat Transfer (perfect gas)

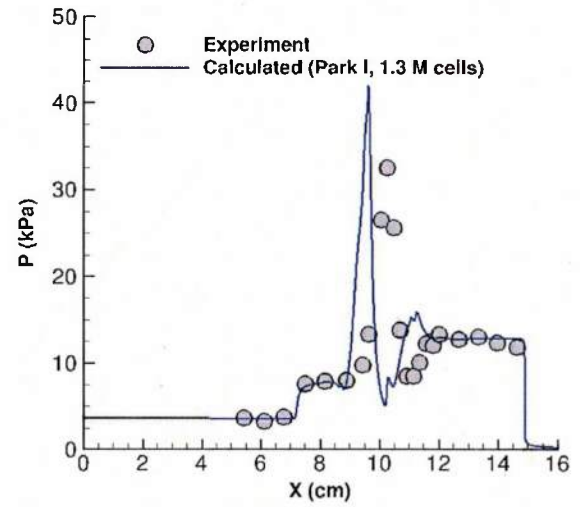


(d) Heat Transfer (Park I)

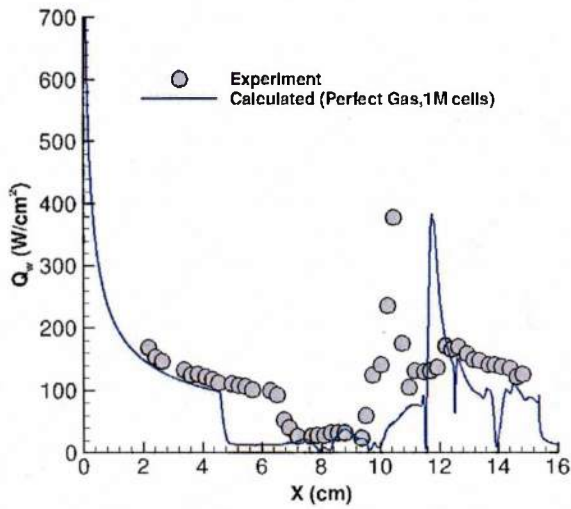
Figure 8: Surface Pressure and Heat Transfer for Run 1 (5.44 MJ/kg)



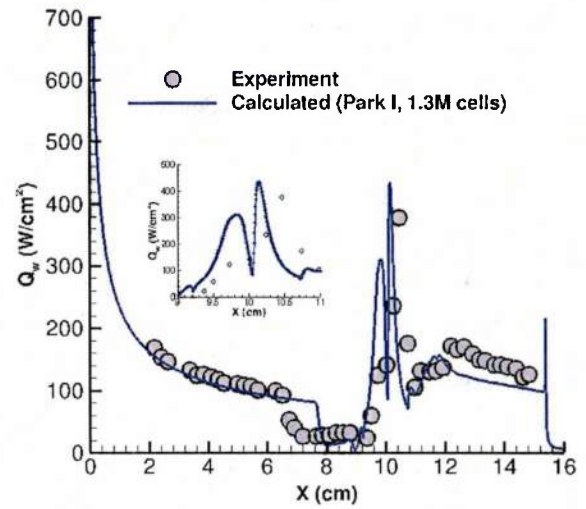
(a) Pressure (perfect gas)



(b) Pressure (Park I)

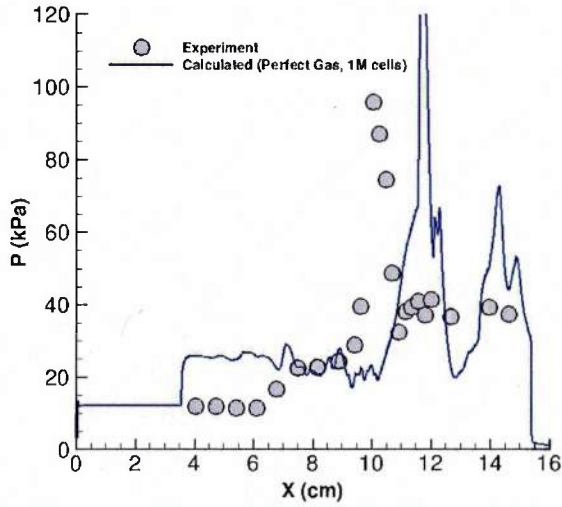


(c) Heat Transfer (perfect gas)

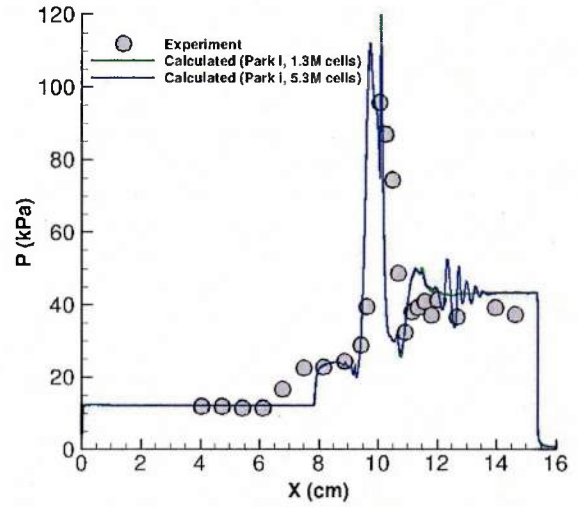


(d) Heat Transfer (Park I)

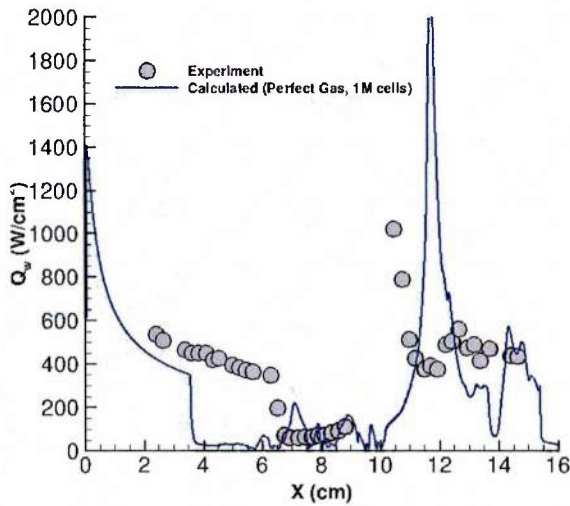
Figure 9: Surface Pressure and Heat Transfer for Run 2 (9.65 MJ/kg)



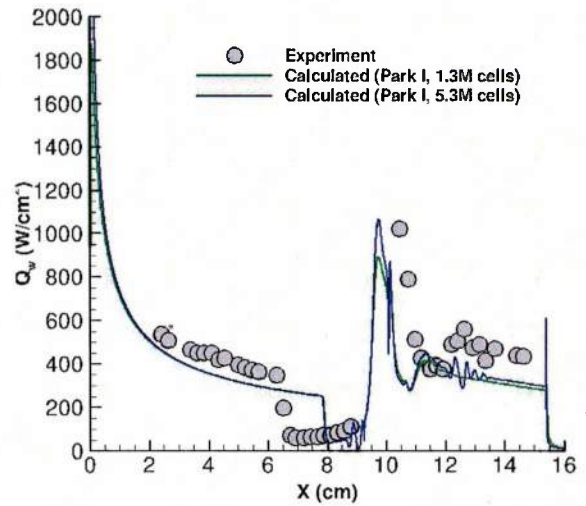
(a) Pressure (perfect gas)



(b) Pressure (Park I)

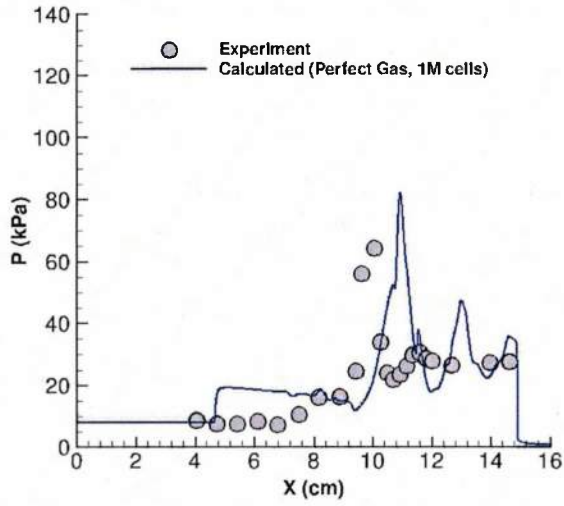


(c) Heat Transfer (perfect gas)

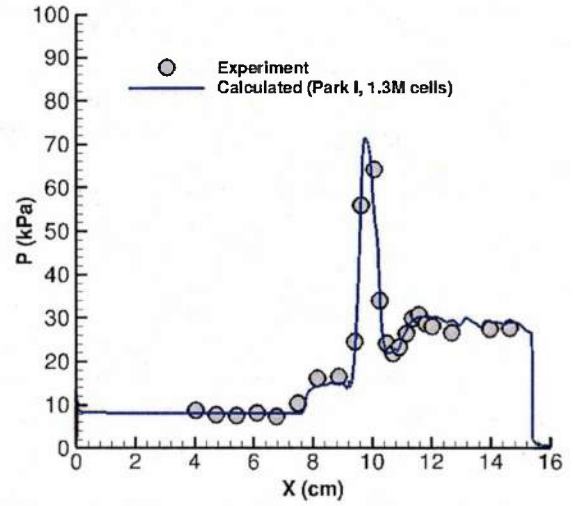


(d) Heat Transfer (Park I)

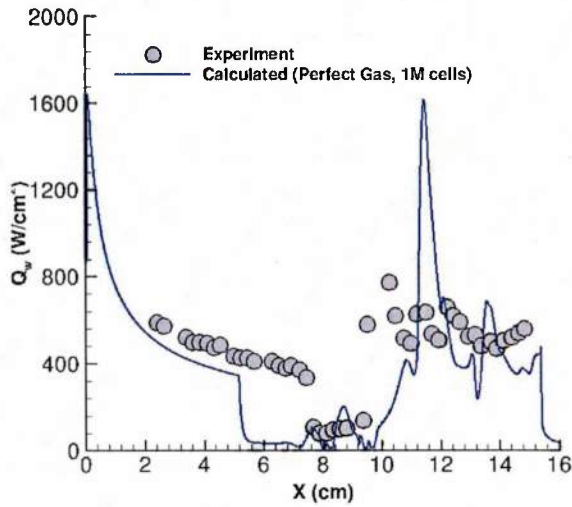
Figure 10: Surface Pressure and Heat Transfer for Run 6 (15.23 MJ/kg)



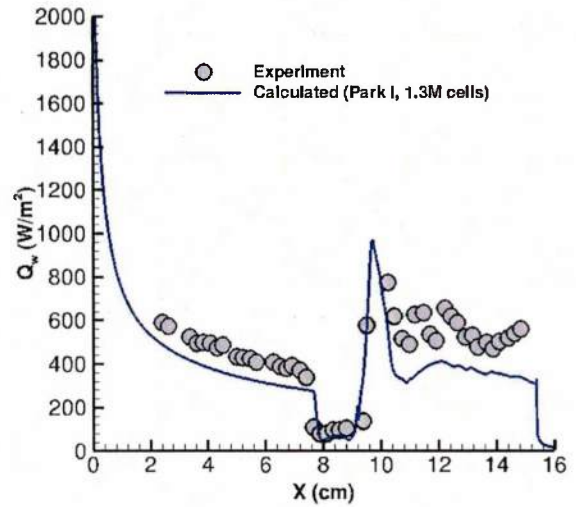
(a) Pressure (perfect gas)



(b) Pressure (Park I)



(c) Heat Transfer (perfect gas)



(d) Heat Transfer (Park I)

Figure 11: Surface Pressure and Heat Transfer for Run 4 (21.77 MJ/kg)

4.1.5 Analysis of Flowfield

Fig. 12 displays contours of species mass fractions of NO, O and N for the 9.65 MJ/kg case². A significant fraction of atomic oxygen O is created by the aft cone shock as indicated in Figs. 12(e,f). The maximum value $Y_O = 0.157$, and the maximum value $Y_O/Y_{O_2} = 4.67$. The mass fraction of atomic nitrogen N is very low, with a maximum mass fraction $Y_N = 0.006$, and hence is not visible in Figs. 12(c,d). The atomic nitrogen N generated by dissociation of N_2 at the aft shock rapidly reacts. The maximum mass fraction $Y_{NO} = 0.084$.

Fig. 13 displays contours of species mass fractions of NO, O and N for the 15.23 MJ/kg case. Similar to the 9.65 MJ/kg case, a significant fraction of atomic oxygen O is created by the aft cone shock as indicated in Figs. 13(e,f). The maximum value $Y_O = 0.2346$, and the maximum value $Y_O/Y_{O_2} = 1942$. Nearly all of the molecular oxygen O_2 is dissociated by the high temperatures generated by the aft cone shock, with the mass fraction Y_{O_2} substantially below 1% downstream of the aft cone shock. The mass fraction of atomic nitrogen N increases downstream of the aft cone shock in comparison with the 9.65 MJ/kg case, with a maximum mass fraction $Y_N = 0.084$. The maximum mass fraction $Y_{NO} = 0.088$.

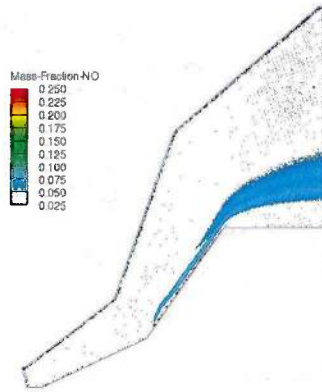
Fig. 14 displays contours of species mass fractions of NO, O and N for the 21.77 MJ/kg case. Similar to the 9.65 MJ/kg and 15.23 MJ/kg cases, a significant fraction of atomic oxygen O is created by the aft cone shock as indicated in Figs. 14(e,f). The maximum value $Y_O = 0.2349$, and the maximum value $Y_O/Y_{O_2} = 2.60 \cdot 10^4$, indicating effectively all molecular oxygen O_2 has been dissociated at some point downstream of the aft cone shock. The mass fraction of atomic nitrogen N increases downstream of the aft cone shock in comparison with the 9.65 MJ/kg and 15.23 MJ/kg cases, with a maximum mass fraction $Y_N = 0.184$. The maximum mass fraction $Y_{NO} = 0.093$.

The difference between the vibrational temperature³ and translational-rotational temperature $T_{vib} - T$ for the 9.65 MJ/kg, 15.23 MJ/kg and 21.77 MJ/kg cases is displayed in Fig. 15. In the incoming flow, $T_{vib} = T$. The vibrational temperature remains relatively frozen throughout the interaction, and consequently $T_{vib} - T$ is negative immediately downstream of the aft cone shock, and positive downstream of the expansion corner.

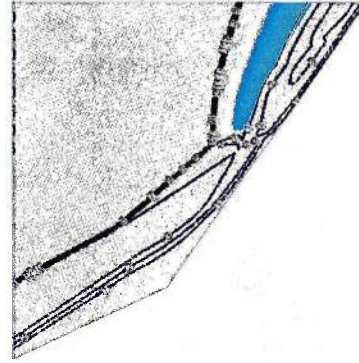
²The mass fraction scale is the same for all cases and species.

³The averaged vibrational temperature T_{avg}^{vib} is determined assuming an equilibrium vibrational distribution at the averaged vibrational energy e_{avg}^{vib} defined as

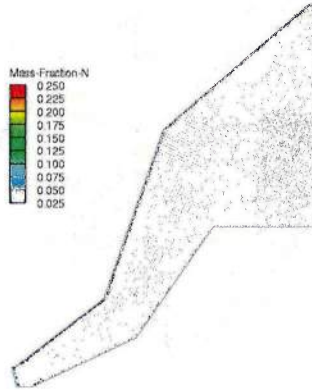
$$e_{avg}^{vib} = \sum_{\alpha=1}^m Y_{\alpha} e_{\alpha}^{vib}$$



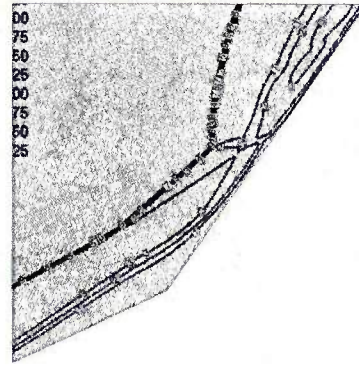
(a) Y_{NO}



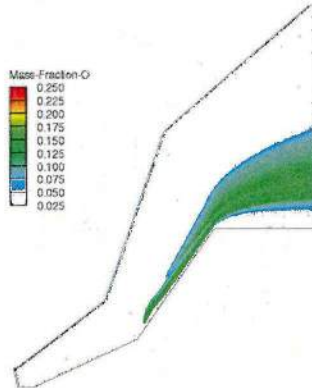
(b) Y_{NO} and Mach isolines



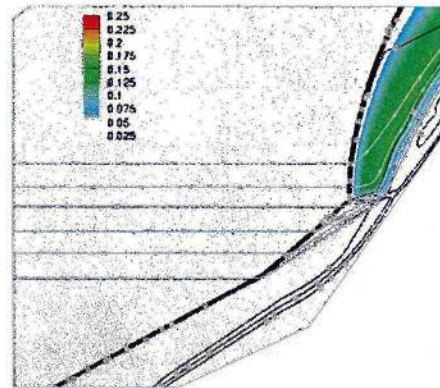
(c) Y_N



(d) Y_N and Mach isolines

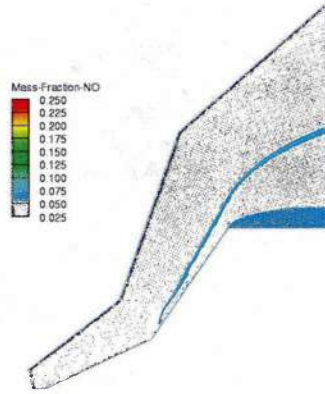


(e) Y_O

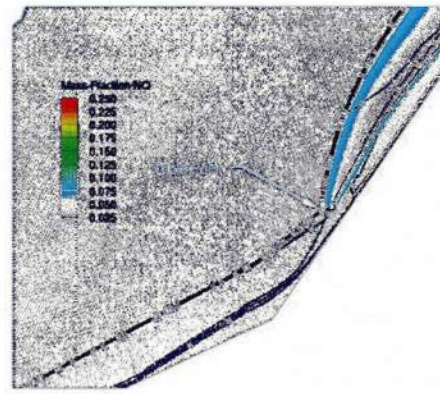


(f) Y_O and Mach isolines

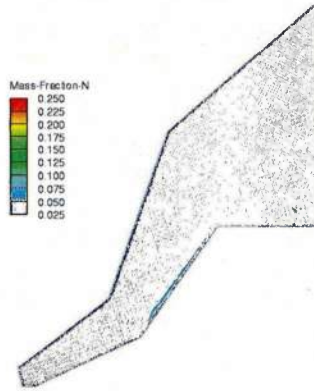
Figure 12: Species mass fractions for Park I (9.65 MJ/kg)



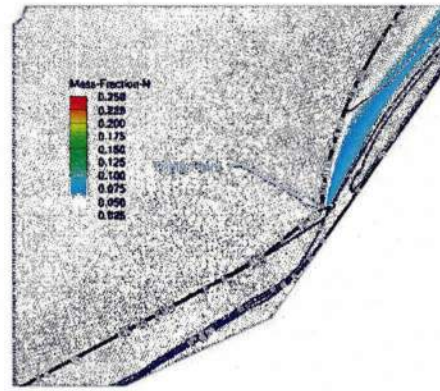
(a) Y_{NO}



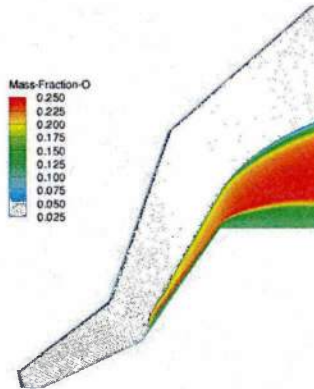
(b) Y_{NO} and Mach isolines



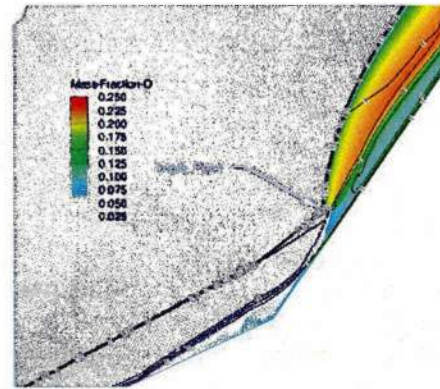
(c) Y_N



(d) Y_N and Mach isolines

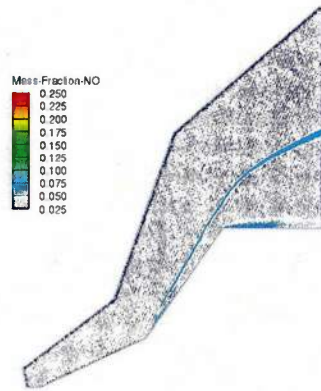


(e) Y_O

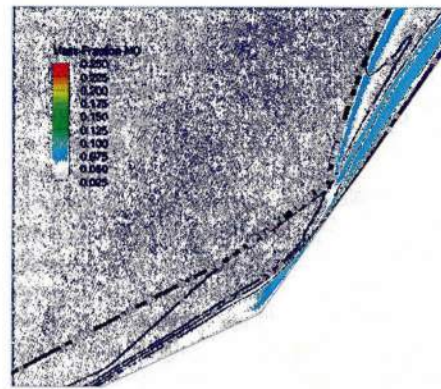


(f) Y_O and Mach isolines

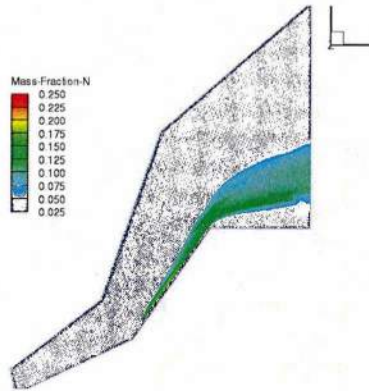
Figure 13: Species mass fractions for Park I (15.23 MJ/kg)



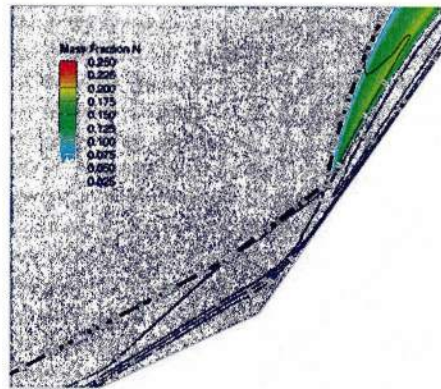
(a) Y_{NO}



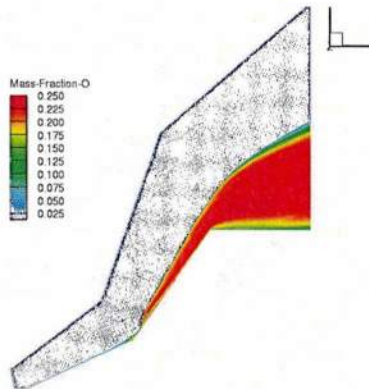
(b) Y_{NO} and Mach isolines



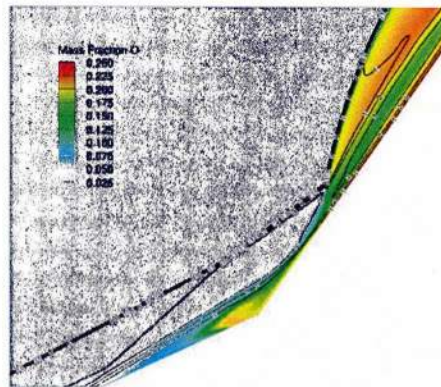
(c) Y_N



(d) Y_N and Mach isolines

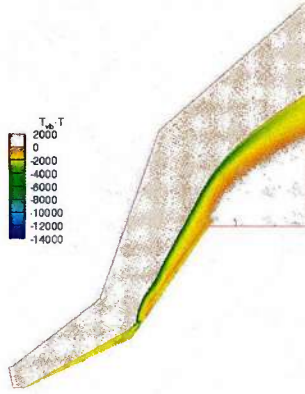


(e) Y_O

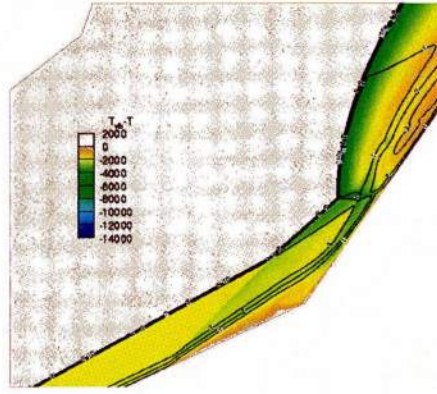


(f) Y_O and Mach isolines

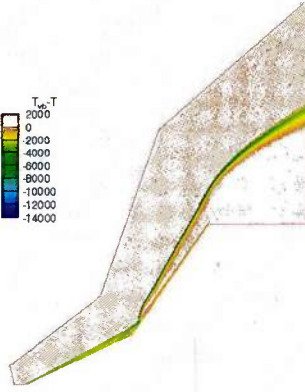
Figure 14: Species mass fractions for Park I (21.77 MJ/kg)



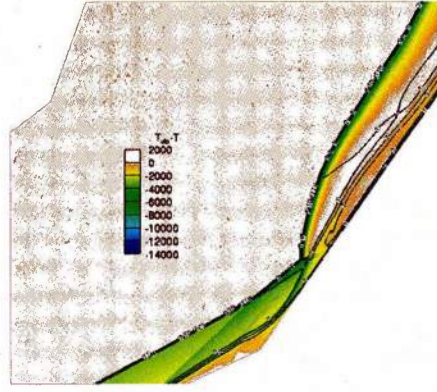
(a) 9.65 MJ/kg



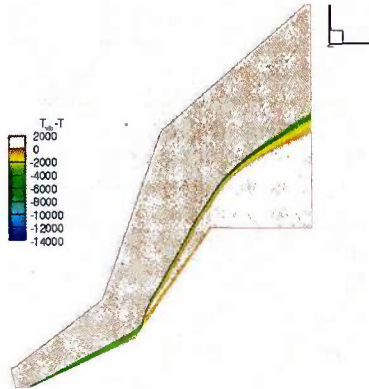
(b) 9.65 MJ/kg



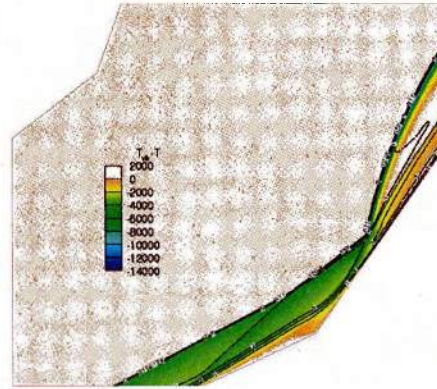
(c) 15.23 MJ/kg



(d) 15.23 MJ/kg



(e) 21.77 MJ/kg



(f) 21.77 MJ/kg

Figure 15: $T_{\text{vib}} - T$ (left) and $T_{\text{vib}} - T$ with Mach isolines (right)

4.2 Hollow Cylinder Flare

Table 5: Hollow Cylinder Flare Simulations

Run No	Total Enthalpy (<i>MJ/kg</i>)	Mach Number	Perfect Gas			Park I	
			1M	4M	16M	1M	4M
1	5.07	11.3	✓	✓	✓		
2	10.43	12.6	✓	✓	✓	✓	
4	15.54	11.5	✓	✓	✓	✓	✓
5	21.85	13.2	✓	✓		✓	

4.2.1 5.07 MJ/kg (Run 1)

The computed and experimental surface pressure and heat transfer for Run 1 (5.07 MJ/kg) are presented in Fig. 16. Figs. 16(a) and 16(b) display the results using the perfect gas model including grid refinement. The computed peak pressure using the perfect gas model exceeds the experiment by 60%. The computed peak heat transfer using the perfect gas model agrees with experiment within the experimental uncertainty; however, the perfect gas simulations overpredict the size of the separation region. The perfect gas simulations demonstrated grid independence as indicated by the results for the three different grids.

4.2.2 10.43 MJ/kg (Run 2)

The computed and experimental surface pressure and heat transfer for Run 2 (10.43 MJ/kg) are presented in Fig. 17. Figs. 17(a) and 17(c) display the results using the perfect gas model including grid refinement. Figs. 17(b) and 17(d) display the results of non-equilibrium gas using the Park I model for 1M cells. The computed peak pressure using the perfect gas model exceeds the experiment by 30%, while the computed peak pressure of the Park I exceeds the experiment by 50%. The computed peak heat transfer using the perfect gas model agrees with experiment within the experimental uncertainty, while the calculated peak heat transfer of Park I model exceeds the experiment by 25%. No separated region is observed in any of the simulations of the perfect gas model which is the same as what is seen in the experiment. However, the simulations with Park I model creates a separation region.

4.2.3 15.54 MJ/kg (Run 4)

The computed and experimental surface pressure and heat transfer for Run 4 (15.54 MJ/kg) are presented in Fig. 18. Figs. 18(a) and 18(c) display the results using the perfect gas model

including grid refinement for three sequence of grids. Figs. 18(b) and 18(d) display the results of non-equilibrium gas using the Park I model including grid refinement for two sequence of grids. The computed peak pressure using both the perfect gas model and Park I model exceeds the experiment by 23%. The computed peak heat transfer using the perfect gas model agrees with experiment within the experimental uncertainty, while the Park I model simulation overestimate the peak heat transfer by 27%. Moreover, the separated region is overpredicted by the perfect gas model while it underpredicted by the Park I model.

4.2.4 21.85 MJ/kg (Run 5)

The computed and experimental surface pressure and heat transfer for Run 5 (21.85 MJ/kg) are presented in Fig. 19. Figs. 19(a) and 19(c) display the results using the perfect gas model including grid refinement for two sequences of grids, and Figs. 19(b) and 19(d) display the results using the non-equilibrium model with Park I reactions. The computed peak pressure using the perfect gas model exceeds the experiment by 87%, while the computed peak pressure using the non-equilibrium model exceeds the experiment by 47%. The computed peak heat transfer using the perfect gas model is within 25% of the experiment while the computed peak heat transfer using the non-equilibrium model agrees with experiment within the experimental uncertainty. The separated region in the simulations using the perfect gas model is larger than experimental data; however the separated region using the Park I model is in good agreement with experiment.

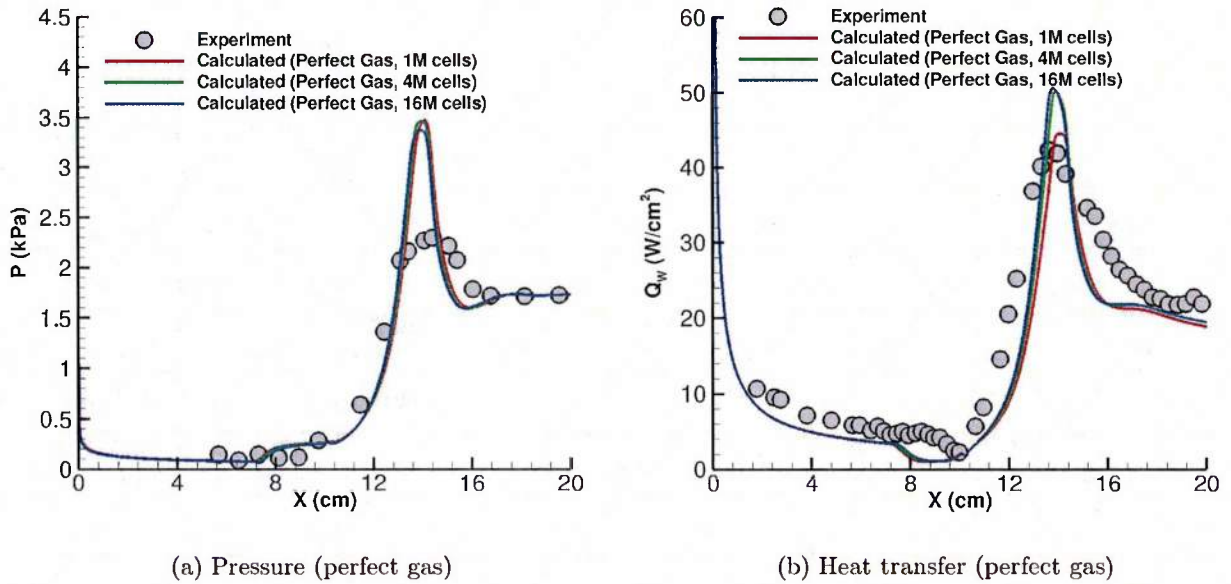
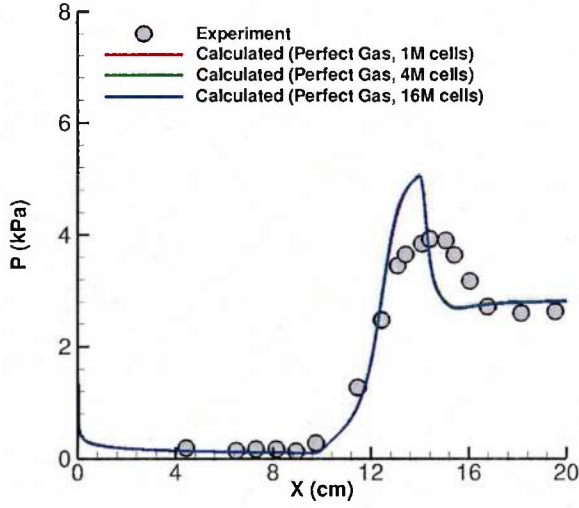
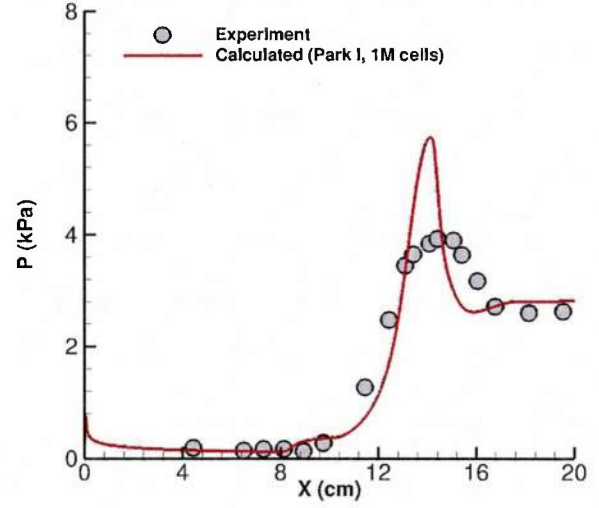


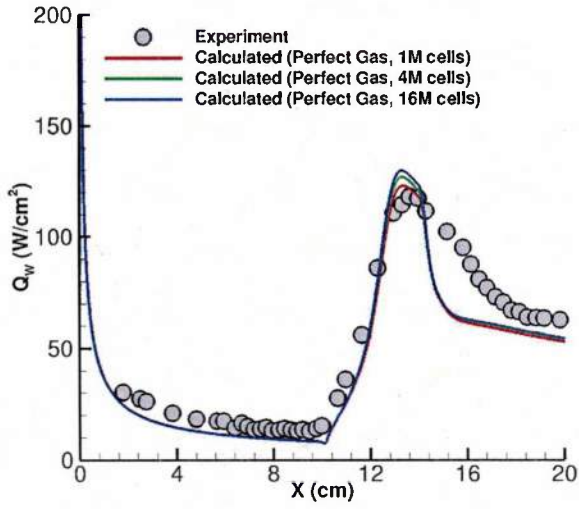
Figure 16: Surface pressure and heat transfer for Run 1 (5.07 MJ/kg)



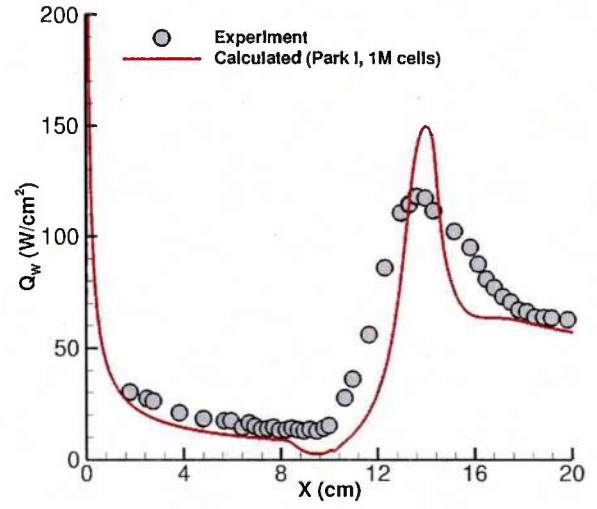
(a) Pressure (perfect gas)



(b) Pressure (Park I)

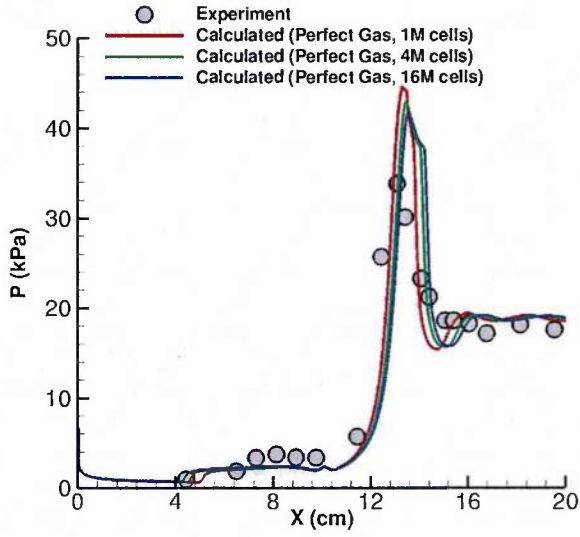


(c) Heat transfer (perfect gas)

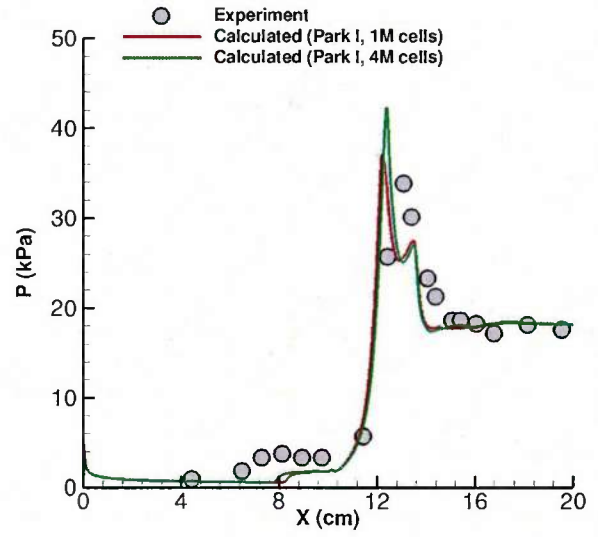


(d) Heat transfer (Park I)

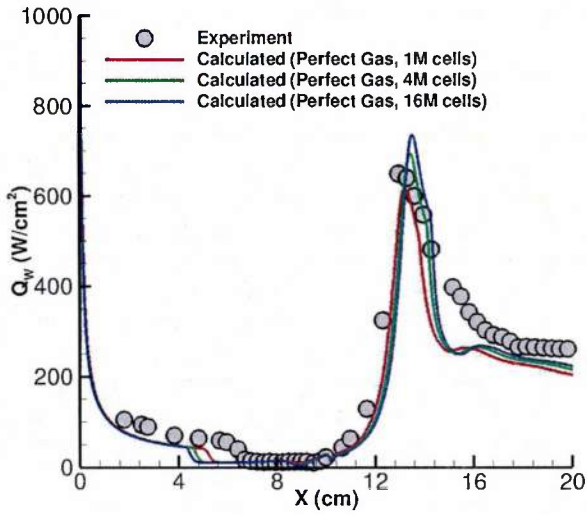
Figure 17: Surface pressure and heat transfer for Run 2 (10.43 MJ/kg)



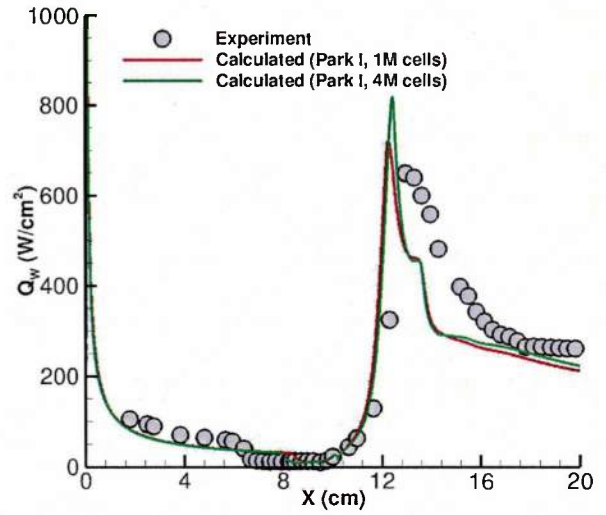
(a) Pressure (perfect gas)



(b) Pressure (Park I)

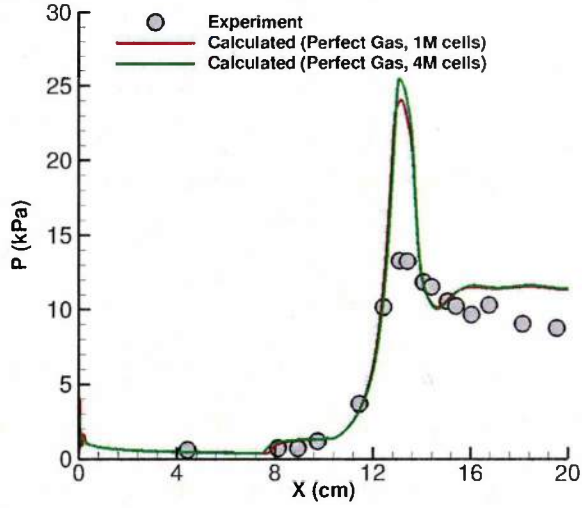


(c) Heat transfer (perfect gas)

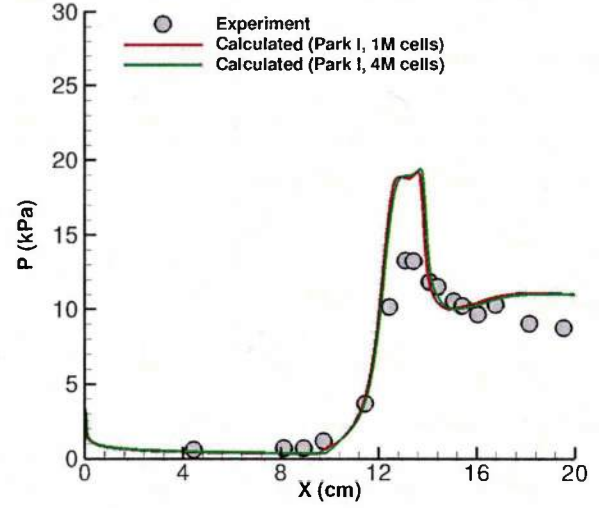


(d) Heat transfer (ParkI)

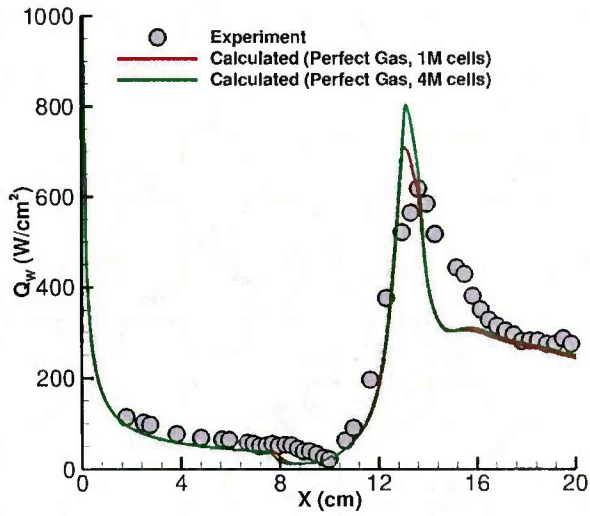
Figure 18: Surface pressure and heat transfer for Run 4 (15.54 MJ/kg)



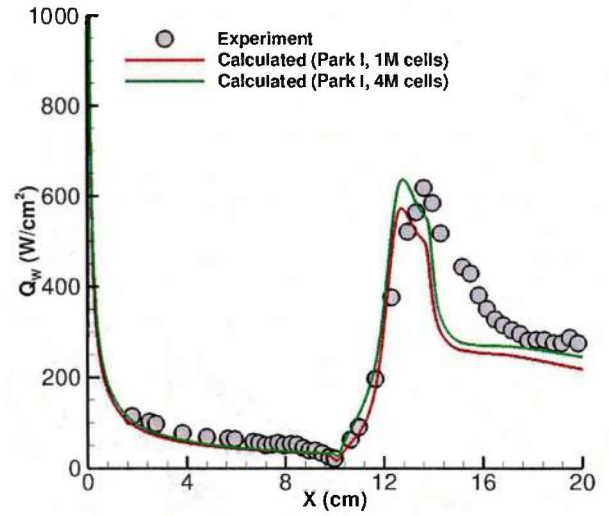
(a) Pressure (perfect gas)



(b) Pressure (Park I)



(c) Heat tranfer (perfect gas)



(d) Heat Transfer (Park I)

Figure 19: Surface pressure and heat transfer for Run 5 (21.85 MJ/kg)

4.2.5 Analysis of Flowfield

Fig. 20 displays the Mach number contours and streamlines for Run 1 (5.07 MJ/kg). Since the 5.07 MJ/kg enthalpy is likely less than what is needed for the gas to dissociate, only the perfect gas model is used for simulation. A recirculation region forms at the cylinder-flare junction due to the adverse pressure gradient. The boundary layer displacement shock, flare shock and separation shock intersect at approximately the location of reattachment.

Fig. 21 shows the Mach number contours and streamlines for Run 2 (10.43 MJ/kg). A surprising result is the absence of a recirculation region at the corner for perfect gas model while the recirculation region exist in non-equilibrium model. In the non-equilibrium simulation the boundary layer displacement shock, flare shock and separation shock intersect at about reattachment point.

Fig. 22 displays the Mach number contours and streamlines for Run 4 (15.54 MJ/kg). A separated region is evident and is significantly larger than for Run 1 (5.07 MJ/kg) in the case of using the perfect gas model. moreover, recirculation region is much more smaller in the non-equilibrium model. For the perfect gas model, the separation shock and boundary layer displacement shock intersect over the recirculation region and the resulting shock intersects the Flare shock in the region above the reattachment point. However, in the non-equilibrium simulation the boundary layer displacement shock and separation shock don't intersect with each other at all and they intersect with flare shock in different location.

Fig. 23 shows the Mach number contours and streamlines for Run 5 (21.85 MJ/kg). The separation region is reduced in size compared to Run 4 in the perfect gas model while the separation region is completely vanished in non-equilibrium simulation with the Park I model.

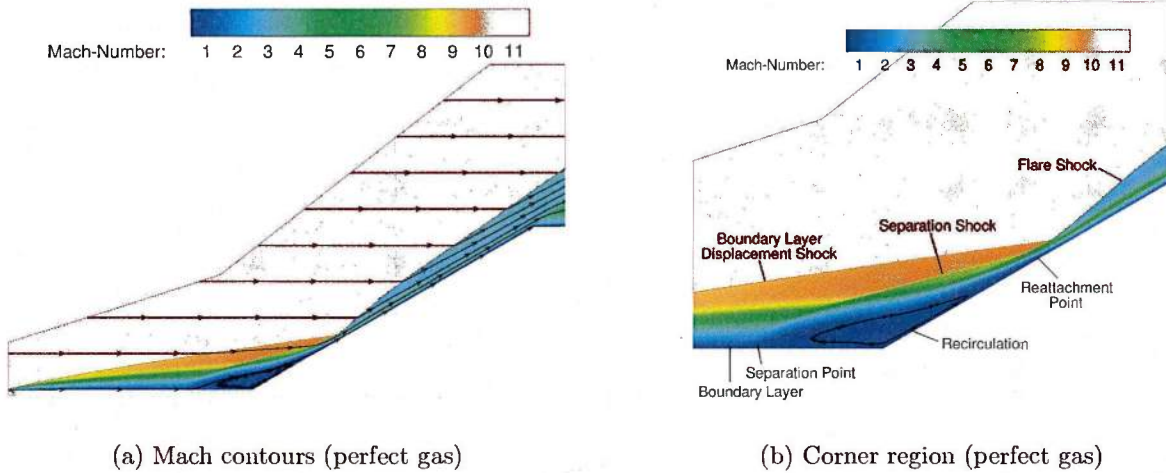
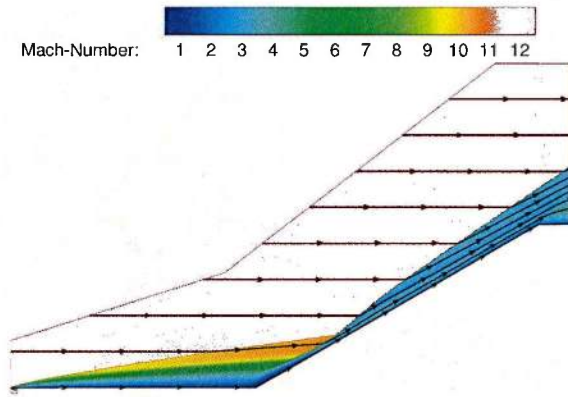
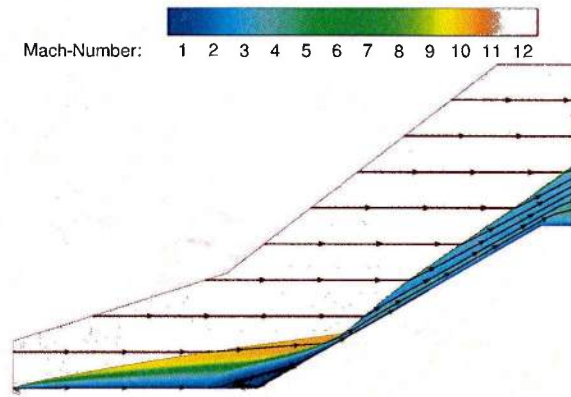


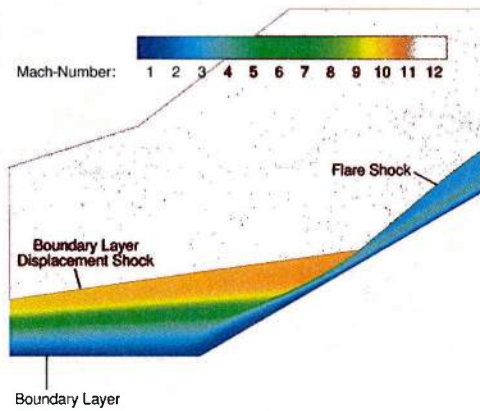
Figure 20: Flow Structure of Run 1 (5.07 MJ/kg)



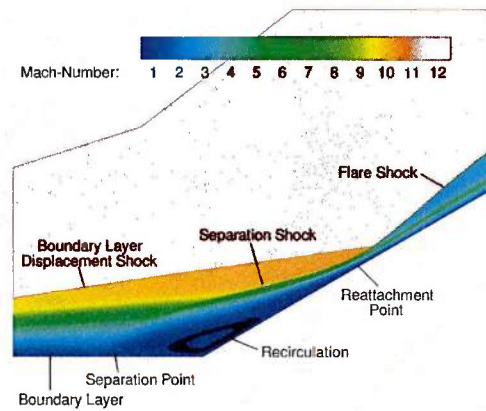
(a) Mach contours (perfect gas)



(b) Mach contours (Park I)

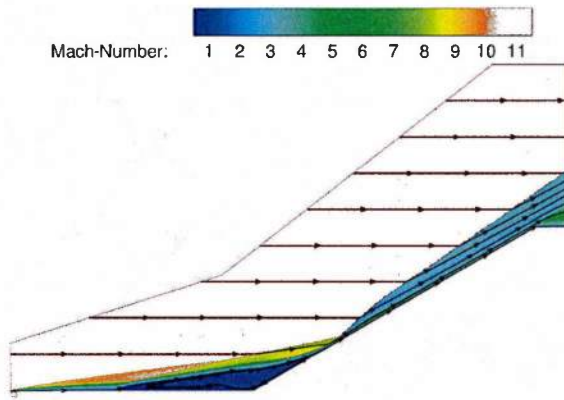


(c) Corner region (perfect gas)

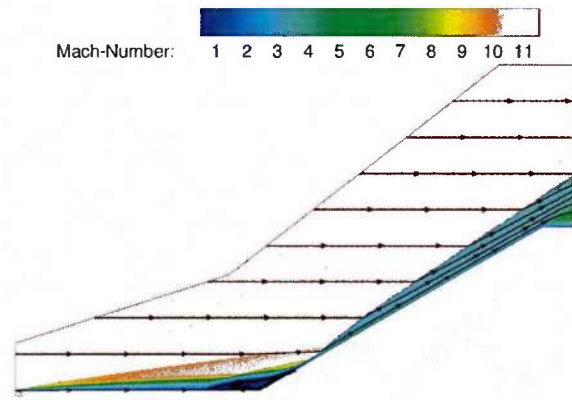


(d) Corner region (Park I)

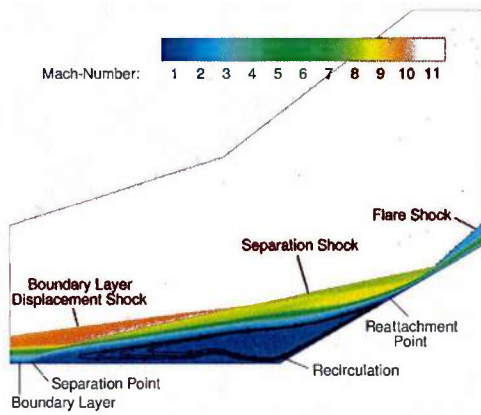
Figure 21: Flow Structure of Run 2 (10.43 MJ/kg)



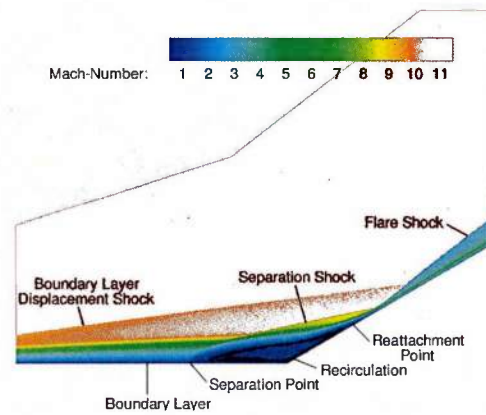
(a) Mach contours (perfect gas)



(b) Mach contours (Park I)

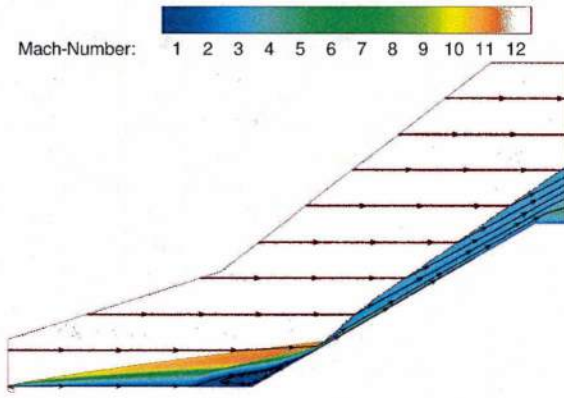


(c) Corner region (perfect gas)

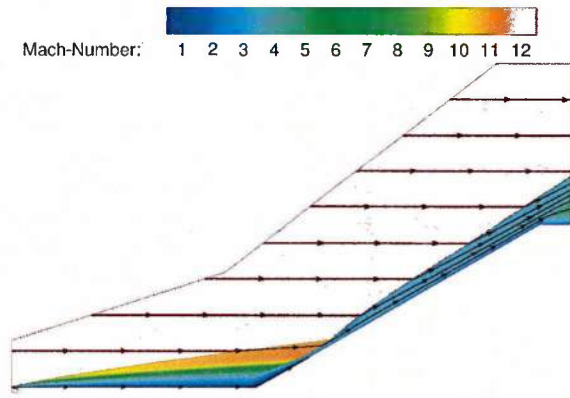


(d) Corner region (Park I)

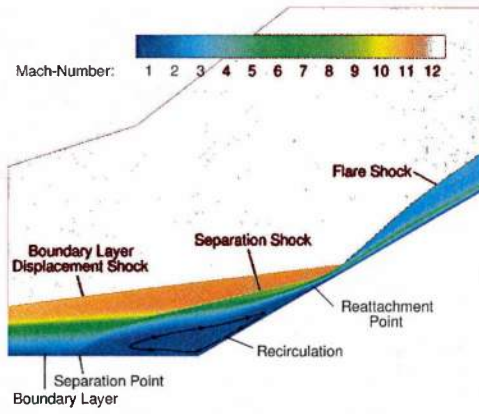
Figure 22: Flow Structure of Run 4 (15.54 MJ/kg)



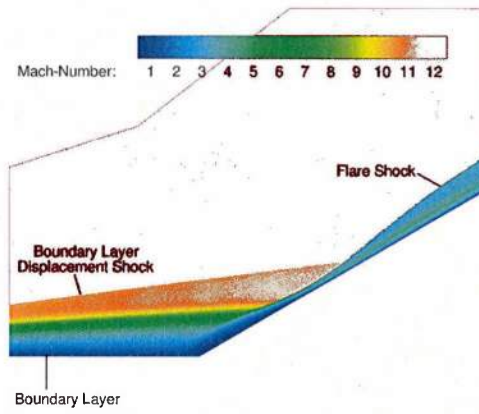
(a) Mach contours (perfect gas)



(b) Mach contours (Park 1)



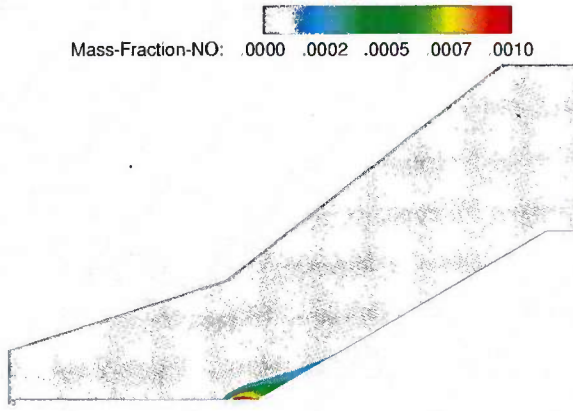
(c) Corner region (perfect gas)



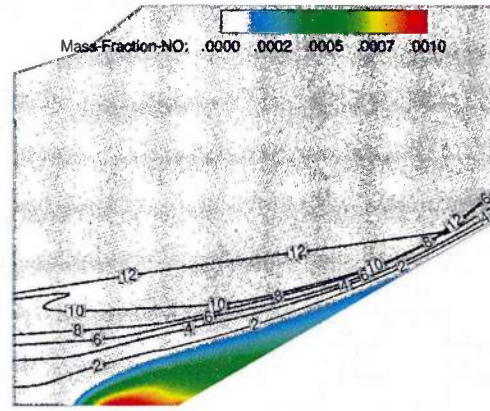
(d) Corner region (Park I)

Figure 23: Flow Structure of Run 5 (21.85 MJ/kg)

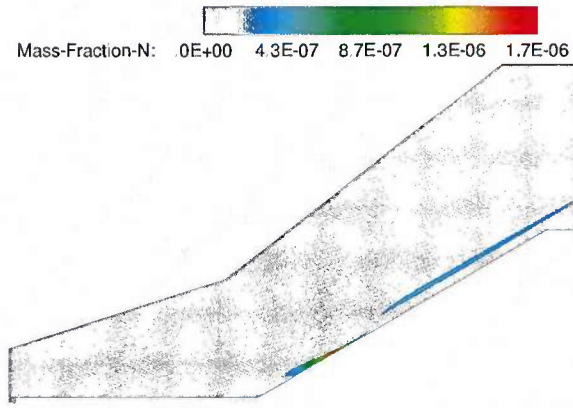
Contours of mass fractions for N, O and NO are displayed in Fig. 24 to 26. Fig. 24 displays the dissociation of N_2 and O_2 occur in the junction of cylinder and flare. The mass fraction of N is very small in relative to mass fraction of NO and O and occurs mostly along the flare. Fig. 25 demonstrates the significant increase in the dissociation of N_2 and O_2 molecules by increasing total enthalpy from 10.43 MJ/kg in Run 2 to 15.54 MJ/kg in Run 4. In this case, most of the mass fraction of NO molecule and N and O atoms appear along the flare especially near the reattachment point. Fig. 26 displays significant dissociation of N_2 and O_2 occur downstream of the reattachment point, and NO rapidly forms. Figs. 28 and 29 display $T_{vib} - T$. The vibrational temperature significantly lags the translational-rotational temperature downstream of the reattachment point.



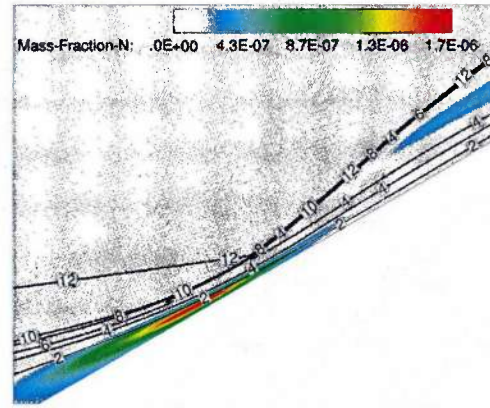
(a) Y_{NO}



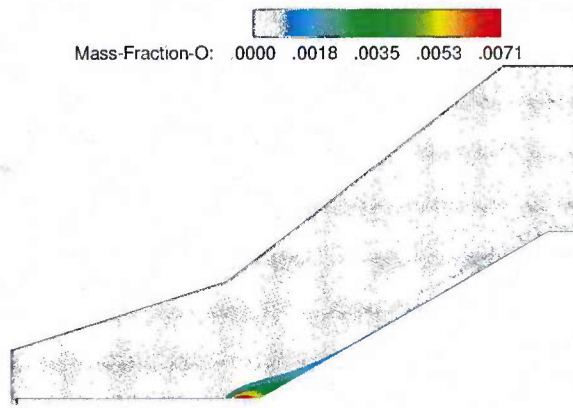
(b) Y_{NO} with constant Mach lines



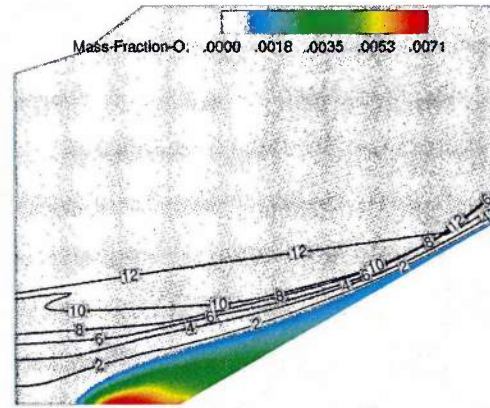
(c) Y_N



(d) Y_N with constant Mach lines

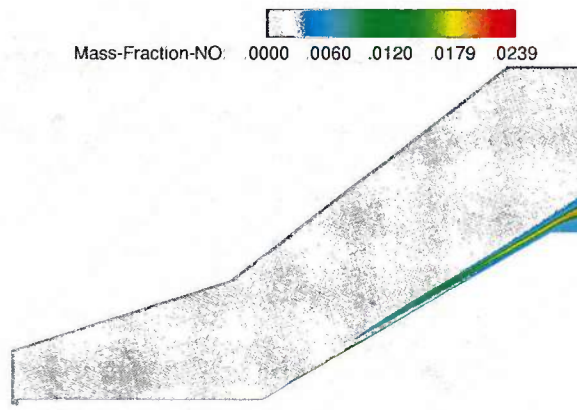


(e) Y_O

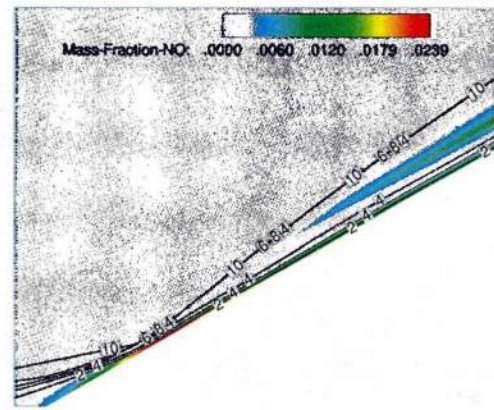


(f) Y_O with constant Mach lines

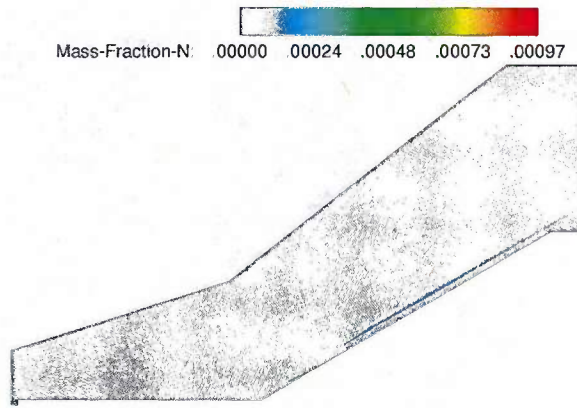
Figure 24: Mass fraction of NO, N and O contours for Run 2 (10.43 MJ/kg)



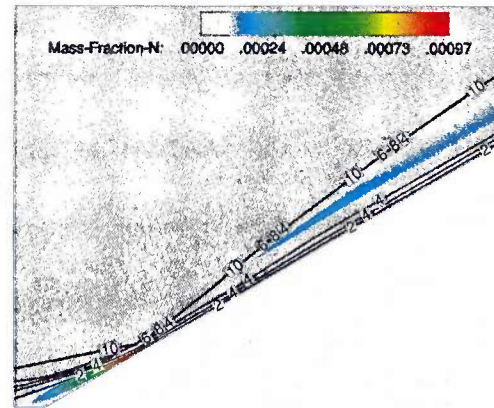
(a) Y_{NO}



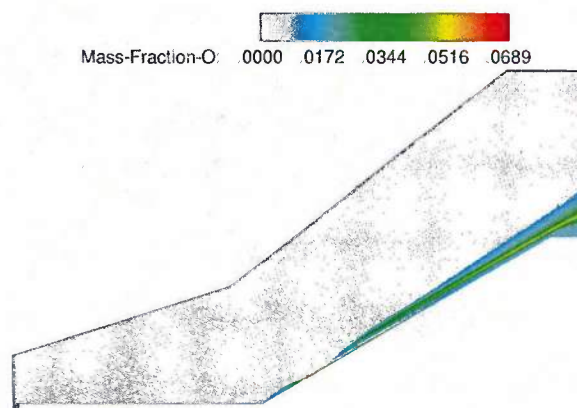
(b) Y_{NO} with constant Mach lines



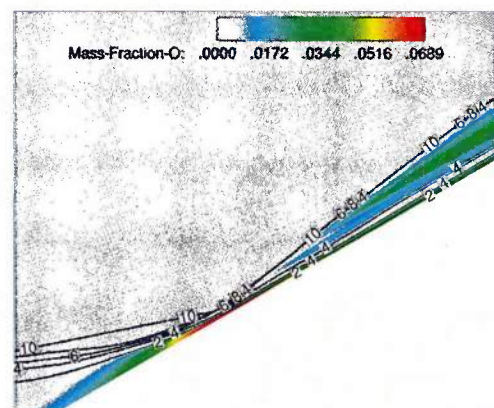
(c) Y_N



(d) Y_N with constant Mach lines

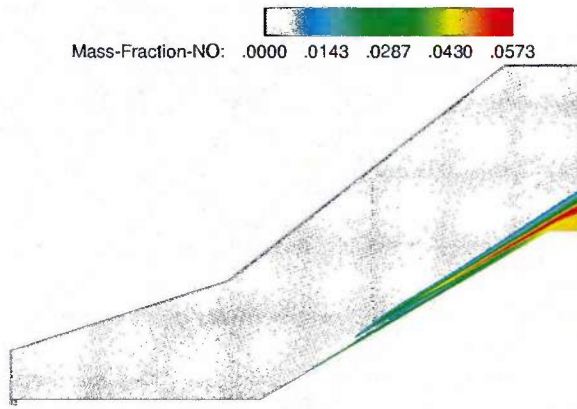


(e) Y_O

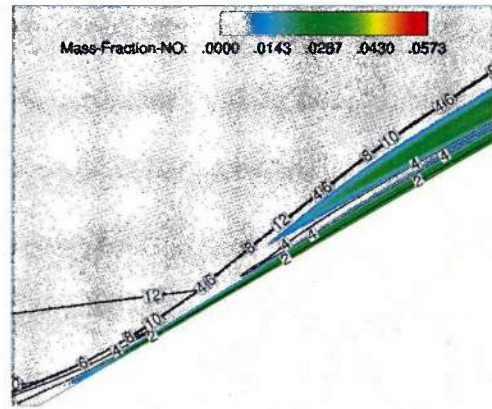


(f) Y_O with constant Mach lines

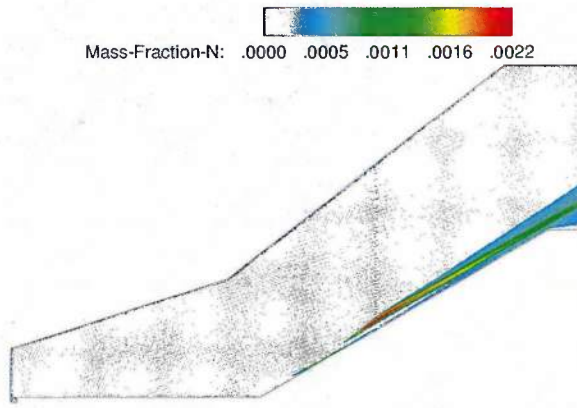
Figure 25: Mass fraction of NO, N and O contours for Run 4 (15.54 MJ/kg)



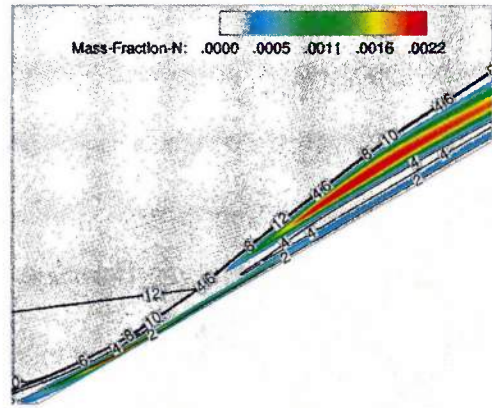
(a) Y_{NO}



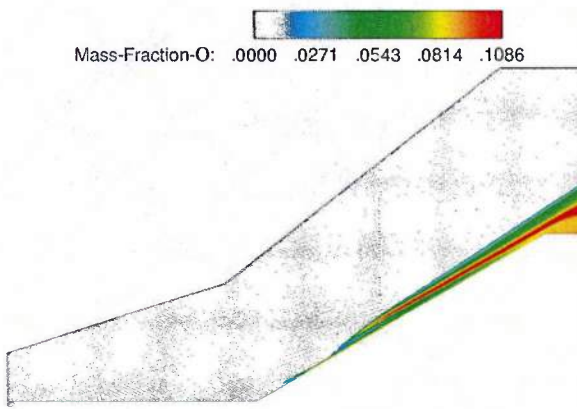
(b) Y_{NO} with constant Mach lines



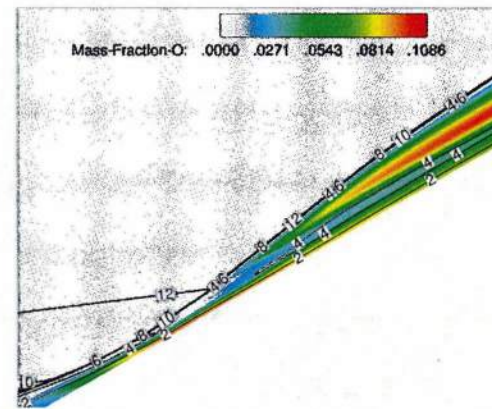
(c) Y_N



(d) Y_N with constant Mach lines

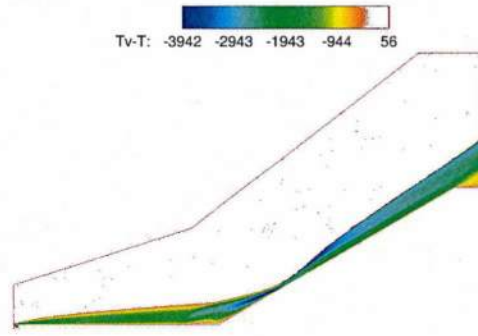


(e) Y_O

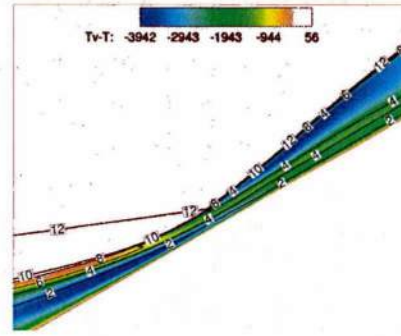


(f) Y_O with constant Mach lines

Figure 26: Mass fraction of NO, N and O contours for Run 5 (21.85 MJ/kg)

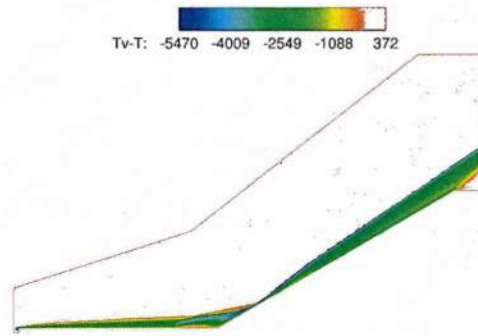


(a) $T^{\text{vib}} - T$ contour

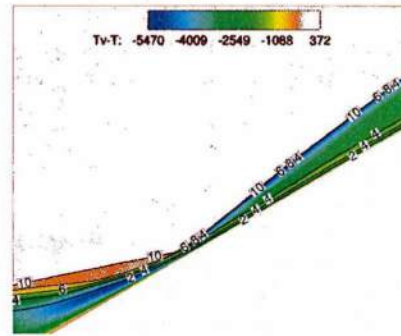


(b) $T^{\text{vib}} - T$ with constant Mach lines

Figure 27: Vibrational temperature contours with Mach lines for Run 2 (10.43 MJ/kg)

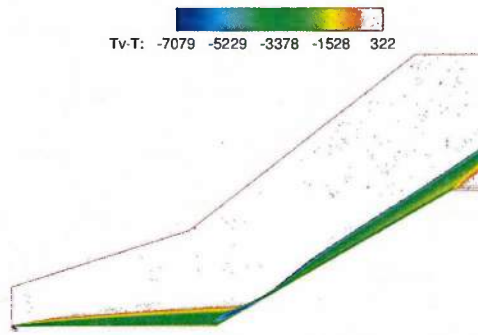


(a) $T^{\text{vib}} - T$ contour

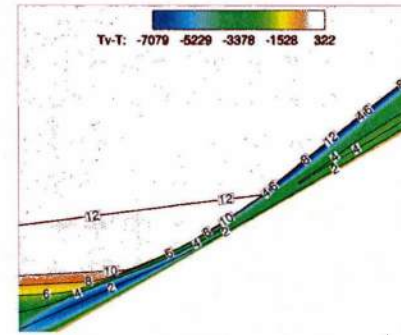


(b) $T^{\text{vib}} - T$ with constant Mach lines

Figure 28: Vibrational temperature contours with Mach lines for Run 4 (15.54 MJ/kg)



(a) $T^{\text{vib}} - T$ contour



(b) $T^{\text{vib}} - T$

Figure 29: Vibrational temperature contours with Mach lines for Run 5 (21.85 MJ/kg)

5 Conclusions, Significance of Results and Transitions

The principal conclusions of the research are

- The Park I model accurately predicts the peak heat flux $\max Q_w$ in nearly all cases
- The Park I model accurately predicts the separation length L_{sep} and peak pressure $\max p$ in approximately one-half of the cases
- The perfect gas model accurately predicts the peak heat flux $\max Q_w$ in all four hollow cylinder flare cases, but in none of the double cone cases
- The perfect gas model accurately predicts the separation length L_{sep} in one case and peak pressure $\max p$ in none of the cases

Table 6: Accuracy of Perfect Gas and Park I Models

Geometry	Run No.	Total Enthalpy (MJ/kg)	Perfect Gas			Park I		
			L_{sep}	$\max p$	$\max Q_w$	L_{sep}	$\max p$	$\max Q_w$
Double Cone	1	5.44	●	○	○	●	○	●
	2	9.65	○	○	○	○	○	●
	6	15.23	○	○	○	○	●	●
	4	21.77	○	○	○	●	●	●
Hollow Cylinder	1	5.07	○	○	●	n/a	n/a	n/a
Flare	2	10.43	○	○	●	●	○	●
	4	15.54	○	○	●	●	●	●
	6	21.85	○	○	●	●	○	●

NOTES:

● Accurate

○ Inaccurate

L_{sep} is the streamwise separation length defined by the Q_w profile

$\max p$ and $\max Q_w$ refer to the peak values of pressure and heat transfer

The significance of the results is:

- The Park I model is a reliable model for prediction of peak heat flux
- The Park I model is not a reliable model for prediction of peak surface pressure or separation length (*i.e.*, surface pressure distribution)

- The perfect gas model is not a reliable model for prediction of peak surface pressure or separation length (*i.e.*, surface pressure distribution) except at the lowest stagnation enthalpy
- The perfect gas model is not a reliable model for prediction of peak heat flux except at the lowest stagnation enthalpy; it is accurate for hollow cylinder flare at all stagnation enthalpies, but not for the double cone

The significance is limited to the types of shock wave laminar boundary layer interactions considered in this study.

6 Personnel

Supported by ONR Grant

Principal Investigator: Professor Doyle Knight

Graduate Research Assistant : Mahsa Mortazavi

Supported by Rutgers University

Graduate Research Assistant : Mehrnaz Rouhi Youseffi

Graduate Research Assistant : Nadia Kianvashrad

7 Publications

7.1 Conference Papers

Rouhi Youseffi, M., and Knight, D., “Assessment of CFD Capability for High Enthalpy Non-Equilibrium Flows with Strong Viscous-Inviscid Interaction”, AIAA SCITECH 2015, AIAA Paper No. 2015-0580, Kissimmee, FL, January 2015.

Kianvashrad, N. and Knight, D., “Simulation of Hypersonic Shock Wave Laminar Boundary Layer Interactions”, Sixth European Conference for Aerospace Sciences, Krakow, Poland, July 2015.

Kianvashrad, N. and Knight, D., “Simulation of Hypersonic Shock Wave Laminar Boundary Layer Interactions on Hollow Cylinder Flare”, accepted for presentation at AIAA SCITECH 2016, San Diego, CA, January 2016.

Mortazavi, M., and Knight, D., “Shock Wave Boundary Layer Interaction in a Hypersonic Laminar Flow on a Hollow Cylinder Flare”, accepted for presentation at AIAA SCITECH 2016, San Diego, CA, January 2016.

7.2 Journal Papers

Kianvashrad, N. and Knight, D., "Simulation of Hypersonic Shock Wave Laminar Boundary Layer Interactions", in preparation.

Mortazavi, M., and Knight, D., "Shock Wave Boundary Layer Interaction in a Hypersonic Laminar Flow on a Hollow Cylinder Flare", in preparation.

Rouhi Youseffi, M., and Knight, D., "Assessment of CFD Capability for High Enthalpy Non-Equilibrium Flows with Strong Viscous-Inviscid Interaction", in preparation.

7.3 Other

Rouhi Youseffi, M., PhD Thesis, in preparation.

8 Point of Contact

Dr. John Spyropoulos
NAVAIR
22195 Elmer Road
Building 106, Floor 2, Room 209B
Patuxent River, MD 20670
Email: John.Spyropoulos@jsf.mil
Tel: 301-757-0489
Fax: 301-757-0562

9 Acknowledgment and Disclaimer

This work was sponsored by the Office of Naval Research, ONR. The views and conclusions contained herein are those of the authors and should not be interpreted as necessarily representing the official policies or endorsements, either expressed or implied, of the Office of Naval Research, or the U.S. government.

10 Metrics

Grant No.: ONR Grant N00014-14-1-0827

Project Title: Assessment of CFD Modeling Capability for Hypersonic Shock Wave Boundary Layer

Final Technical Report for Period: 26 May 2014 - 30 September 2015

Principal Investigator:

Professor Doyle Knight

Department of Mechanical and Aerospace Engineering
Rutgers University - The State University of New Jersey
98 Brett Road · Piscataway, New Jersey 08854
Tel: 732 762 5510 · Fax: 732 445 3124
Email: doyleknight@gmx.com

Date Prepared: 30 November 2015

Number of faculty supported under project during reporting period: 1

Number of postdoctoral researchers supported under project during reporting period: 0

Number of graduate students supported under project during reporting period: 1

Number of undergraduate students supported under project during reporting period: 0

Number of refereed publications during this reporting period for which at least $\frac{1}{3}$ of the work was done under this effort: 4

Number of patents during this reporting period: 0

Number of M.S. students graduated during this reporting period: 0

Number of Ph.D. students graduated during this reporting period: 0

Awards received during this reporting period: 0

References

- [1] Liepmann, H., "The Interaction Between Boundary Layer and Shock Waves in Transonic Flow," *Journal of the Aeronautical Sciences*, Vol. 13, No. 12, 1946, pp. 623–637.
- [2] MacCormack, R., "Numerical Solution of the Interaction of a Shock Wave with a Laminar Boundary Layer," *Lecture Notes in Physics*, Vol. 8, SpringerVerlag, Heidelberg, Germany, 1971, pp. 151–163.
- [3] Shang, J., Hankey, W., and Law, C., "Numerical Simulation of Shock Wave Turbulent Boundary Layer Interaction," *AIAA Journal*, Vol. 14, No. 10, October 1976, pp. 1451–1457.
- [4] Hung, C. and MacCormack, R., "Numerical Solution of Three-Dimensional Shock Wave and Turbulent Boundary-Layer Interaction," *AIAA Journal*, Vol. 16, No. 10, October 1978, pp. 1090–1096.

- [5] Knight, D. and Degrez, G., "Shock Wave Boundary Layer Interactions in High Mach Number Flows - A Critical Survey of Current CFD Prediction Techniques," AGARD Advisory Report AR-319, AGARD, 1998.
- [6] Knight, D., Yan, H., Panaras, A., and Zheltovodov, A., "Advances in CFD Prediction of Shock Wave Turbulent Boundary Layer Interaction," *Progress in Aerospace Sciences*, Vol. 39, 2003, pp. 121–184.
- [7] Knight, D., Longo, J., Drikakis, D., Gaitonde, D., Lani, A., Nompelis, I., Reimann, B., and Walpot, L., "Assessment of CFD Capability for Prediction of Hypersonic Shock Interactions," *Progress in Aerospace Sciences*, Vol. 48–49, 2012, pp. 8–26.
- [8] Knight, D. and Chazot, O., "Assessment of Predictive Capabilities for Aerodynamic Heating of Hypersonic Systems," Final report, in publication, NATO Research and Technology Organization, 2015.
- [9] Dufrene, A., MacLean, M., Parker, R., Wadhams, T., Mundy, E., and Holden, M., "Characterication of the New LENS Expansion Tunnel Facility," AIAA Paper 2010-1564, American Institute of Aeronautics and Astronautics, January 2010.
- [10] Dufrene, A., MacLean, M., Parker, R., and Holden, M., "Experimental Characterization of the LENS Expansion Tunnel Facility including Blunt Body Surface Heating," AIAA Paper 2011-626, American Institute of Aeronautics and Astronautics, January 2011.
- [11] MacLean, M., Private Communication, 22 November 2015.
- [12] Park, C., "On Convergence of Computation of Chemically Reacting Flow," AIAA Paper 1985-0247, American Institute of Aeronautics and Astronautics, January 1985.
- [13] Svehla, R. and McBride, B., "Fortran IV Computer Program for the Calculation of Thermodynamic and Transport Properties of Complex Chemical Systems," NASA TN D-7056, January 1973.
- [14] Vincenti, W. and Kruger, C., *Introduction to Physical Gas Dynamics*, Krieger Publishing Company, Malabar, Florida, 1965.
- [15] Millikan, R. and White, D., "Systematics of Vibrational Relaxation," *Journal of Chemical Physics*, Vol. 39, 1953, pp. 3209–3213.
- [16] "GASP and GASPex Version 5.1.2 Reference Guides," Aerosoft, Inc., Blacksburg, VA, 2014.
- [17] Roe, P., "Approximate Reimann Solvers, Parameter Vectors, and Difference Schemes," *Journal of Computational Physics*, Vol. 43, 1981, pp. 357–372.

- [18] Leer, B. V., "Towards the Ultimate Conservative Difference Scheme III. Upstream-Centered Finite Difference Schemes for Ideal Compressible Flow," *Journal of Computational Physics*, Vol. 23, 1977, pp. 263–275.
- [19] Park, S. and Kwon, J., "An Improved HLLE Method for Hypersonic Viscous Flows," AIAA Paper 2001-2633, American Institute of Aeronautics and Astronautics, June 2001.